Electronic Supporting Information

From Tetranuclear to Pentanuclear [Co–Ln] (Ln = Gd, Tb, Dy, Ho) Complexes Across the Lanthanide Series: Effect of Varying Sequence of Ligand Addition

Dipmalya Basak,[a] Lucy Smythe,[b] Radovan Herchel,[c] Mark Murrie,[b] Ivan Nemec[c,d] and Debashis Ray*[a]

[a]*Department of Chemistry, Indian Institute of Technology, Kharagpur 721 302, India*

[b]*School of Chemistry, University of Glasgow, Glasgow, G12 8QQ, United Kingdom*

[c]*Department of Inorganic Chemistry, Faculty of Science, Palacky University, 17 Listopadu 12, Olomouc CZ-77146, Czech Republic*

[d]*Central European Institute of Technology, CEITEC BUT, Purkyňova 656/123, 61200 Brno, Czech Republic*

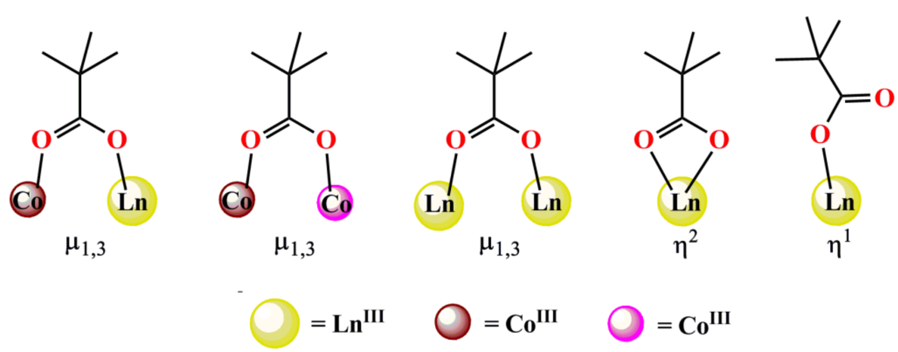

Chart S1 Different binding modes of pivalate ions found in this work.

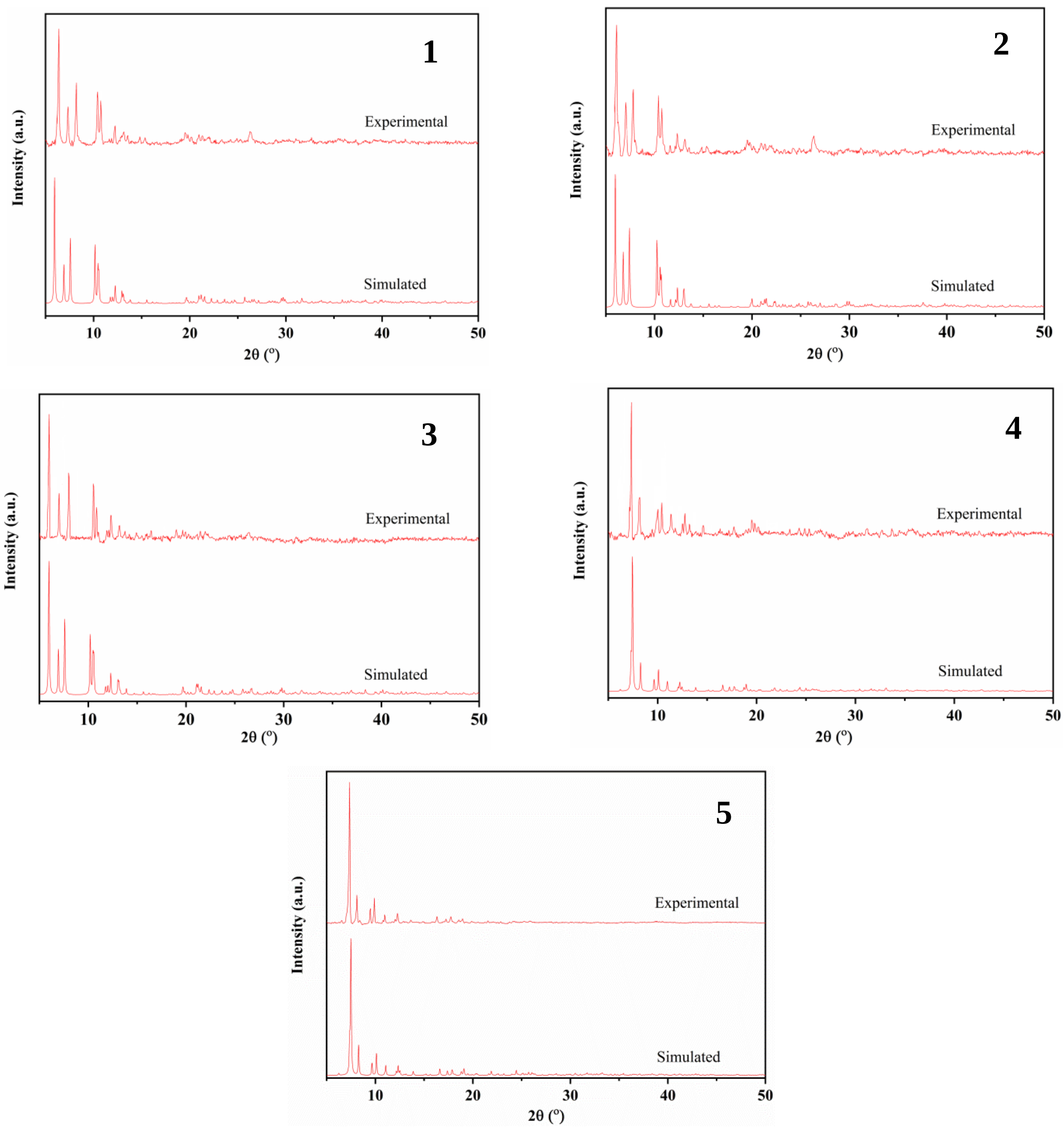

Fig. S1 Experimental and simulated powder X−ray diffraction patterns for **1**−**5**.

Powder X−Ray Diffraction Patterns

The powder XRD patterns of the bulk materials of **1**–**5**, collected using a Bruker AXS X–ray diffractometer, were compared with the simulations derived from the single crystal X–ray diffraction data. Figure S1 shows that the experimental powder patterns are in good agreement with the simulated ones. The difference in intensity is due to the orientation of the powder samples during experiment. The similarity infers that the prepared powder samples are pure and have comparable composition to that of the single crystals. It is to be noted that the measurements were carried out immediately after collecting the bulk material from the crystallization mixture.

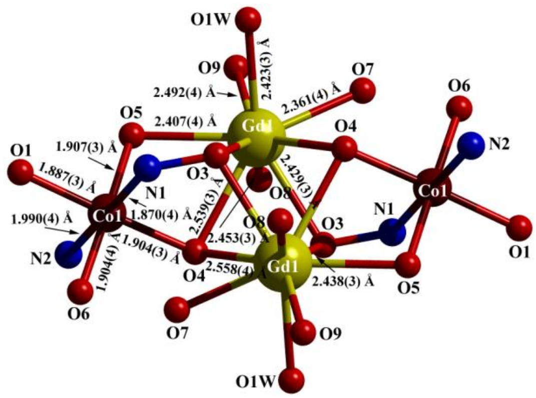

Fig. S2 Core structure of **1** showing important bond distances. Color code: Co^{III} brown, Gd^{III} yellow, N blue, and O red.

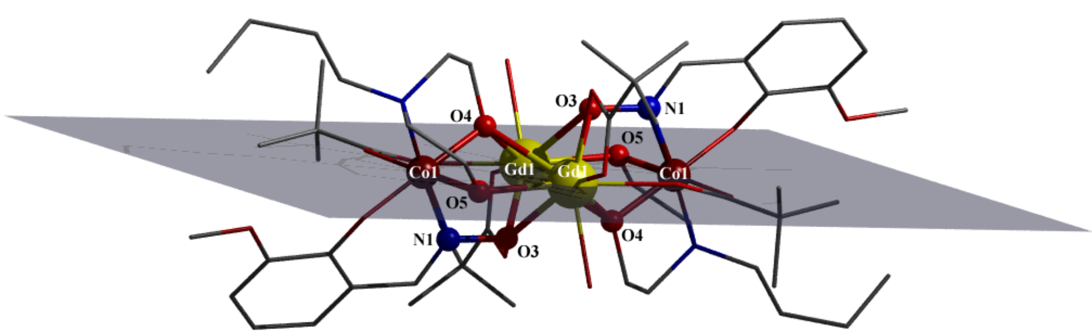

Fig. S3 Positioning of metal ion centers and bridging O atoms with respect to the plane (grey blue) containing two Gd1 and two Co1 in **1**. Color code: Co^{III} brown, Gd^{III} yellow, N blue, O red, and C grey.

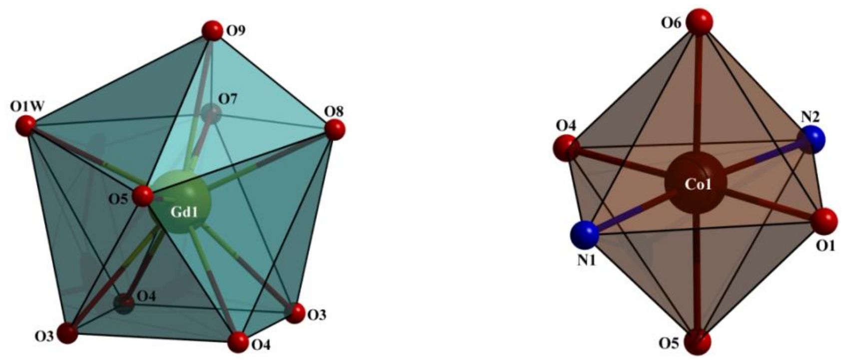

(a) **(b)**

Fig. S4 Geometries around Gd1 and Co1 in **1** as a representative example: (a) Distorted Muffin, (b) Distorted Octahedron. Both **2** and **3** exhibit similar geometries around Ln^{III} and Co^{III} centers.

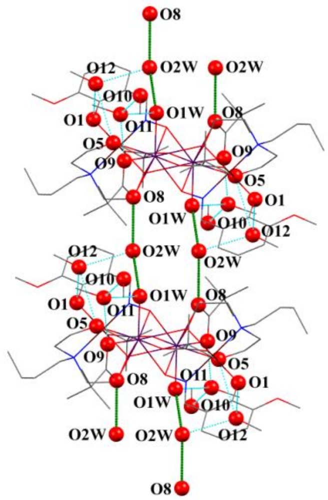

Fig. S5 Hydrogen bonded infinite 1D chain structure formed with the help of lattice H_2O molecules in **3**. The green lines represent the direction of growth of the chain while the trapping of MeOH molecules are shown by light blue lines.

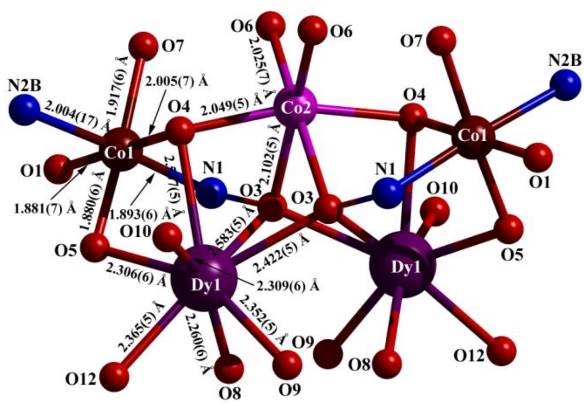

Fig. S6 Core structure of **4** showing important bond distances. Color code: Co^{III} brown, Co^{II} pink, Dy^{III} violet, N blue, and O red.

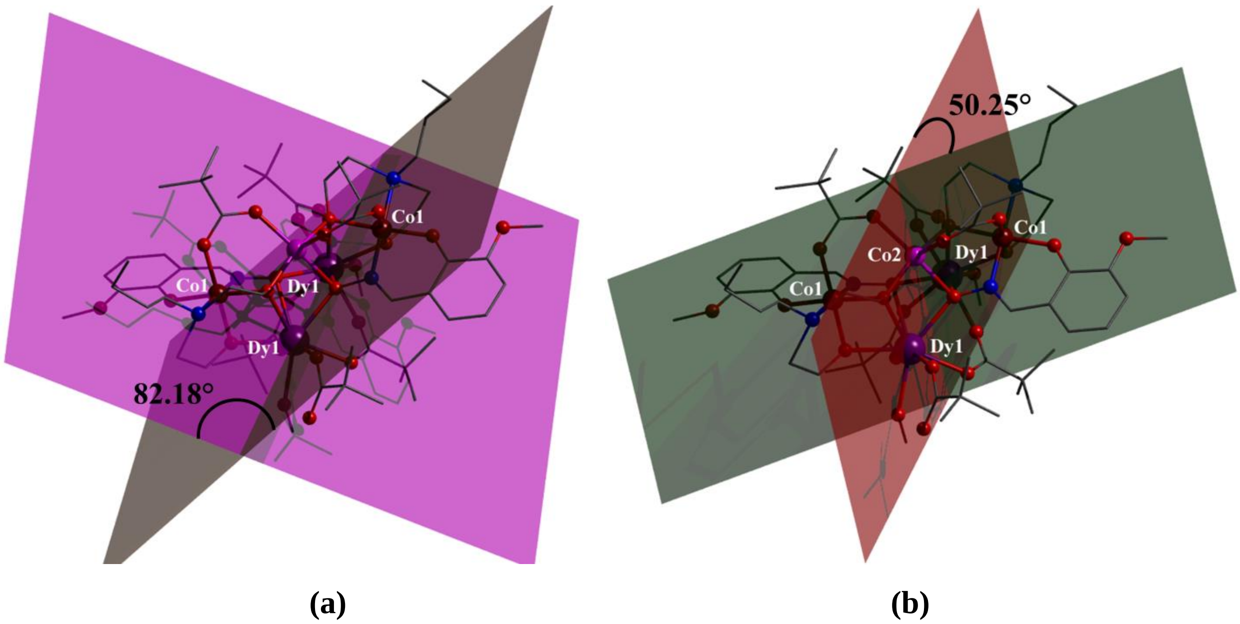

Fig. S7 Spatial orientation of the planes containing (a) one Co1 and two Dy1, (b) two Co1, one Co2 and two Dy1, one Co2 in **4**. Color code: Co^{III} brown, Co^{II} pink, Dy^{III} violet, N blue, O red, and C grey.

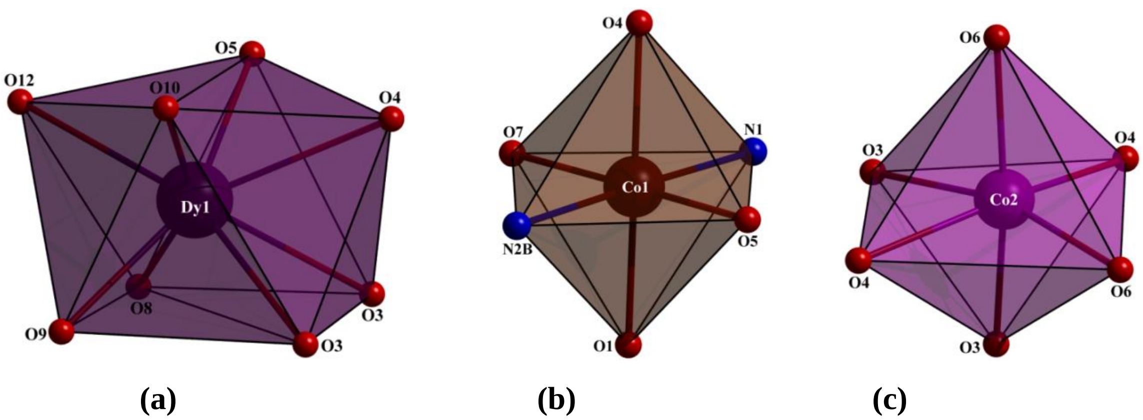

Fig. S8 Geometries around Dy1, Co1 and Co2 in **4** as a representative example: (a) Distorted Square Antiprism, (b) and (c) Distorted Octahedron. **5** exhibits similar geometries around Ho^{III}, Co^{II} and Co^{III} centers.

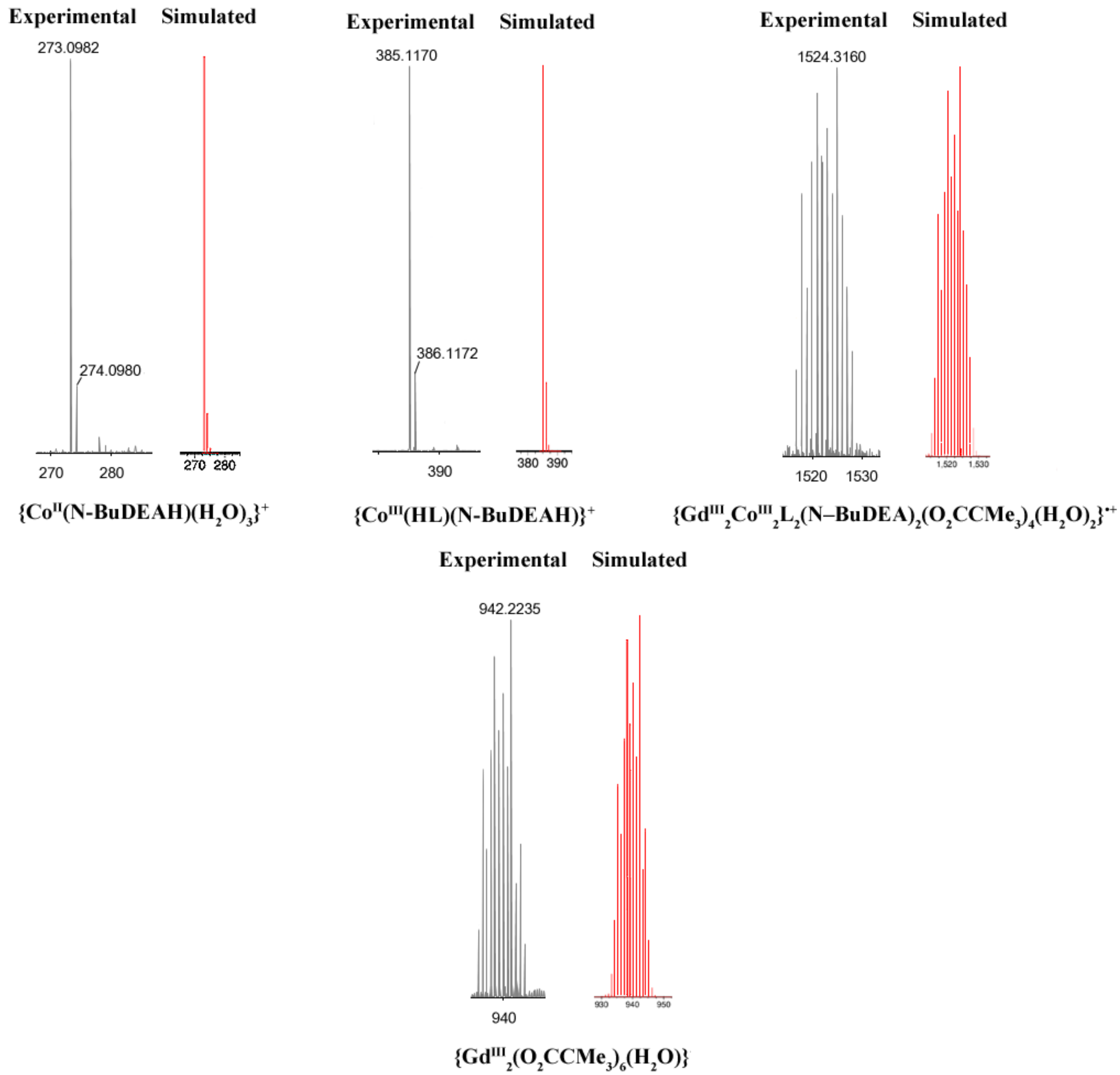

Fig. S9 Experimental and simulated peaks corresponding to different species present in solution obtained from HRMS (+ve) for addition of N–BuDEAH_2 before H_2L during synthesis of **1** in MeOH.

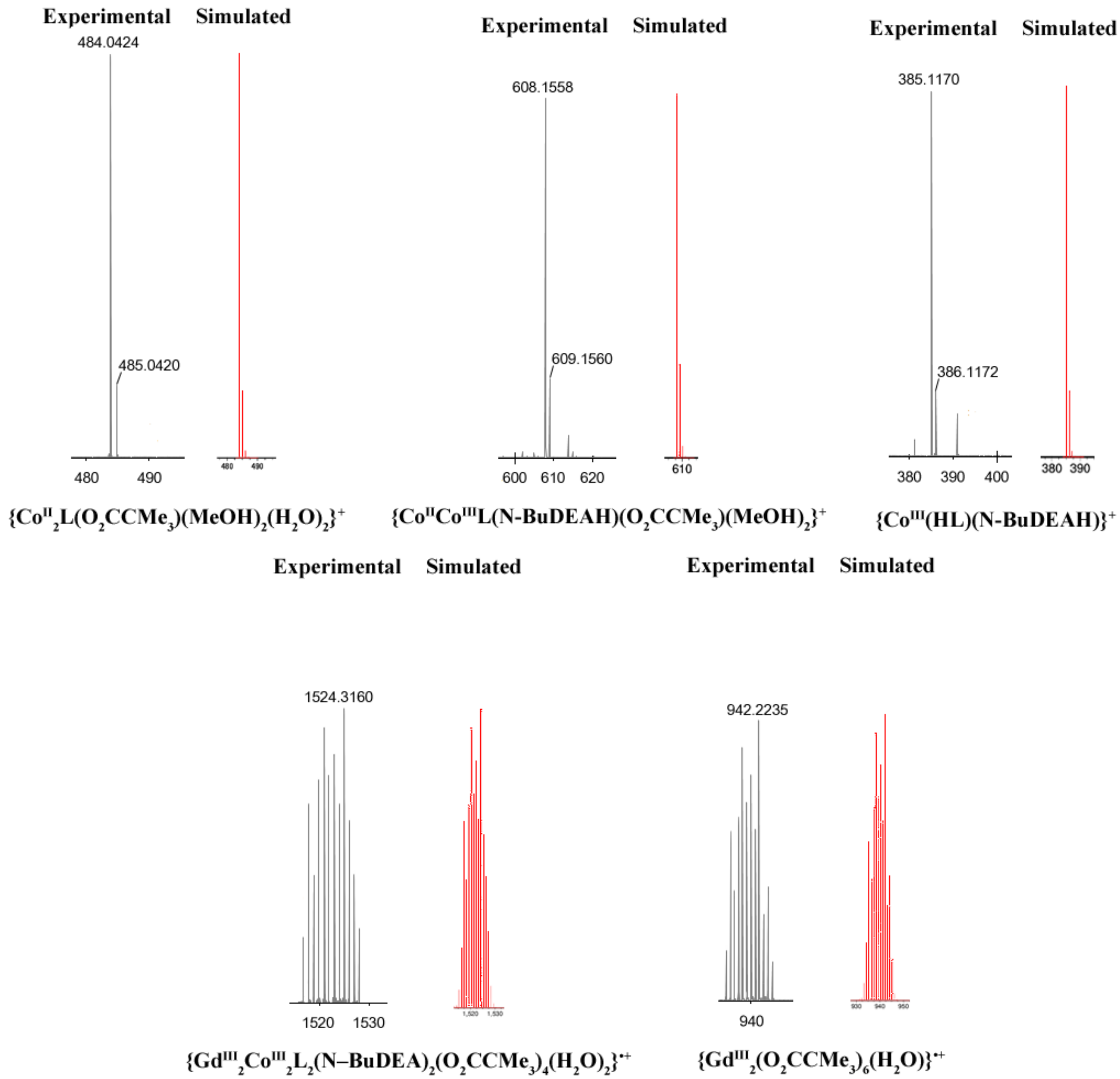

Fig. S10 Experimental and simulated peaks corresponding to different species present in solution obtained from HRMS (+ve) for addition of H_2L before N−BuDEAH$_2$ during synthesis of **1** in MeOH.

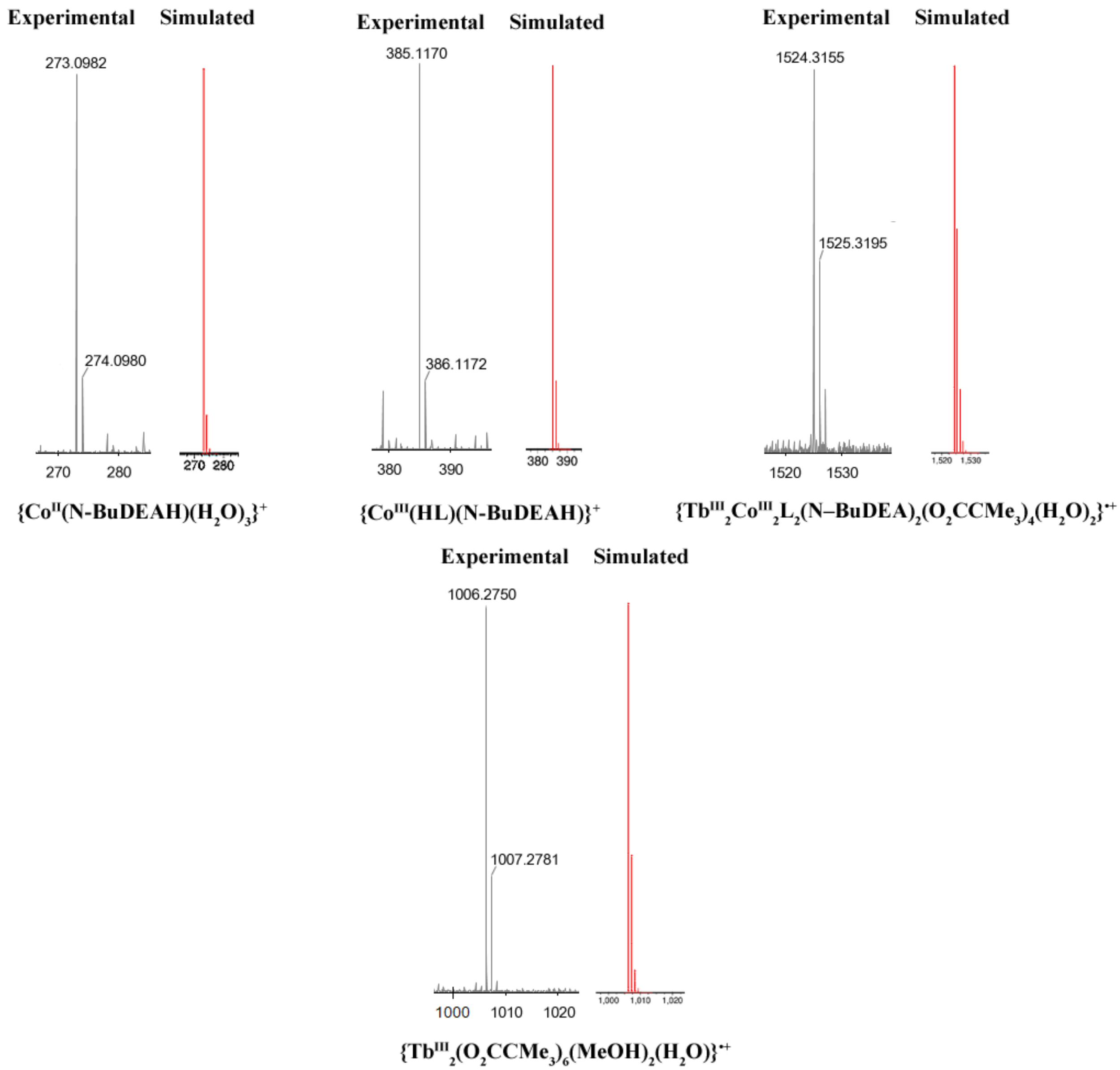

Fig. S11 Experimental and simulated peaks corresponding to different species present in solution obtained from HRMS (+ve) for addition of N−BuDEAH$_2$ before H$_2$L during synthesis of **2** in MeOH.

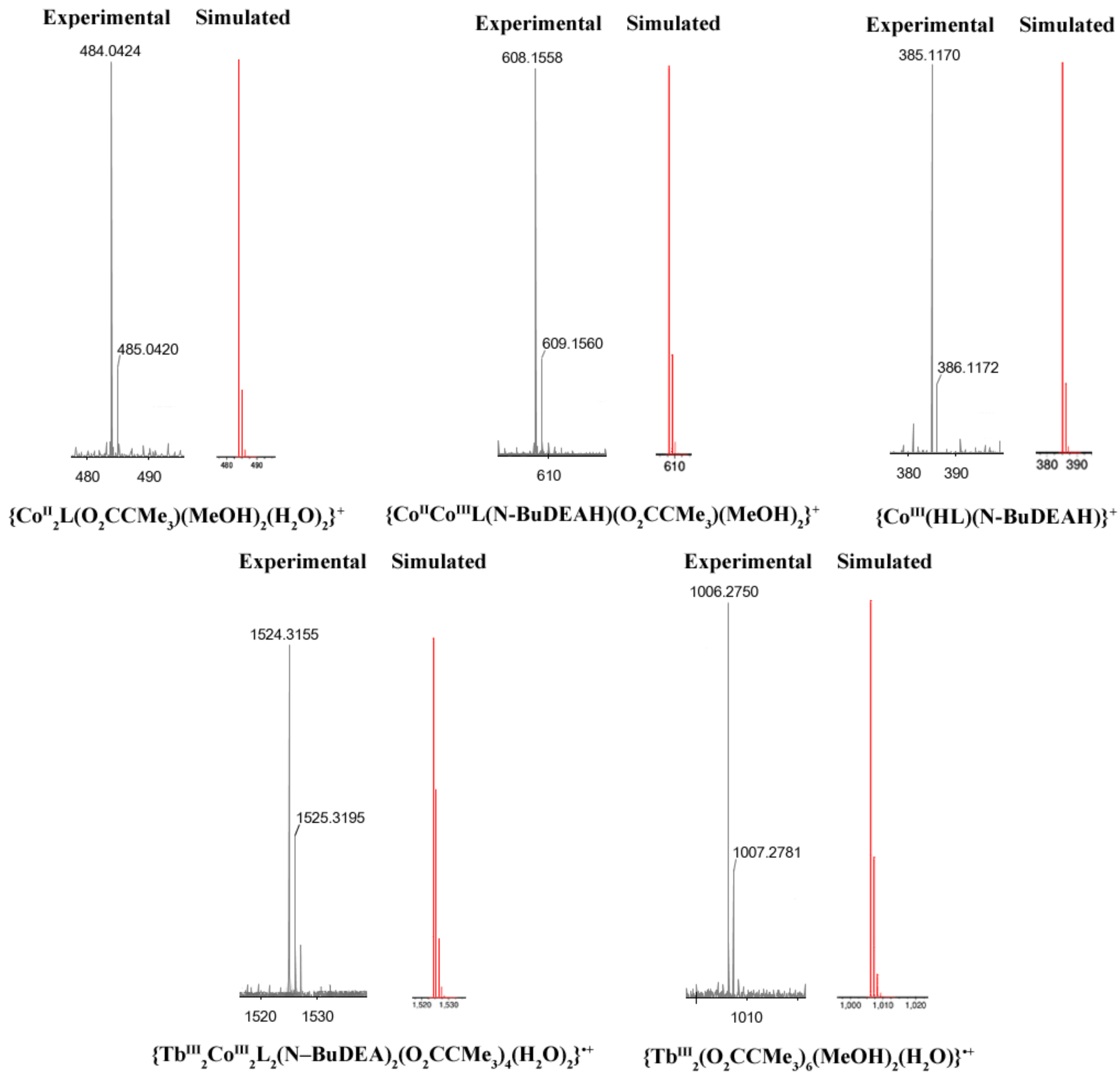

Fig. S12 Experimental and simulated peaks corresponding to different species present in solution obtained from HRMS (+ve) for addition of H_2L before N–BuDEAH_2 during synthesis of **2** in MeOH.

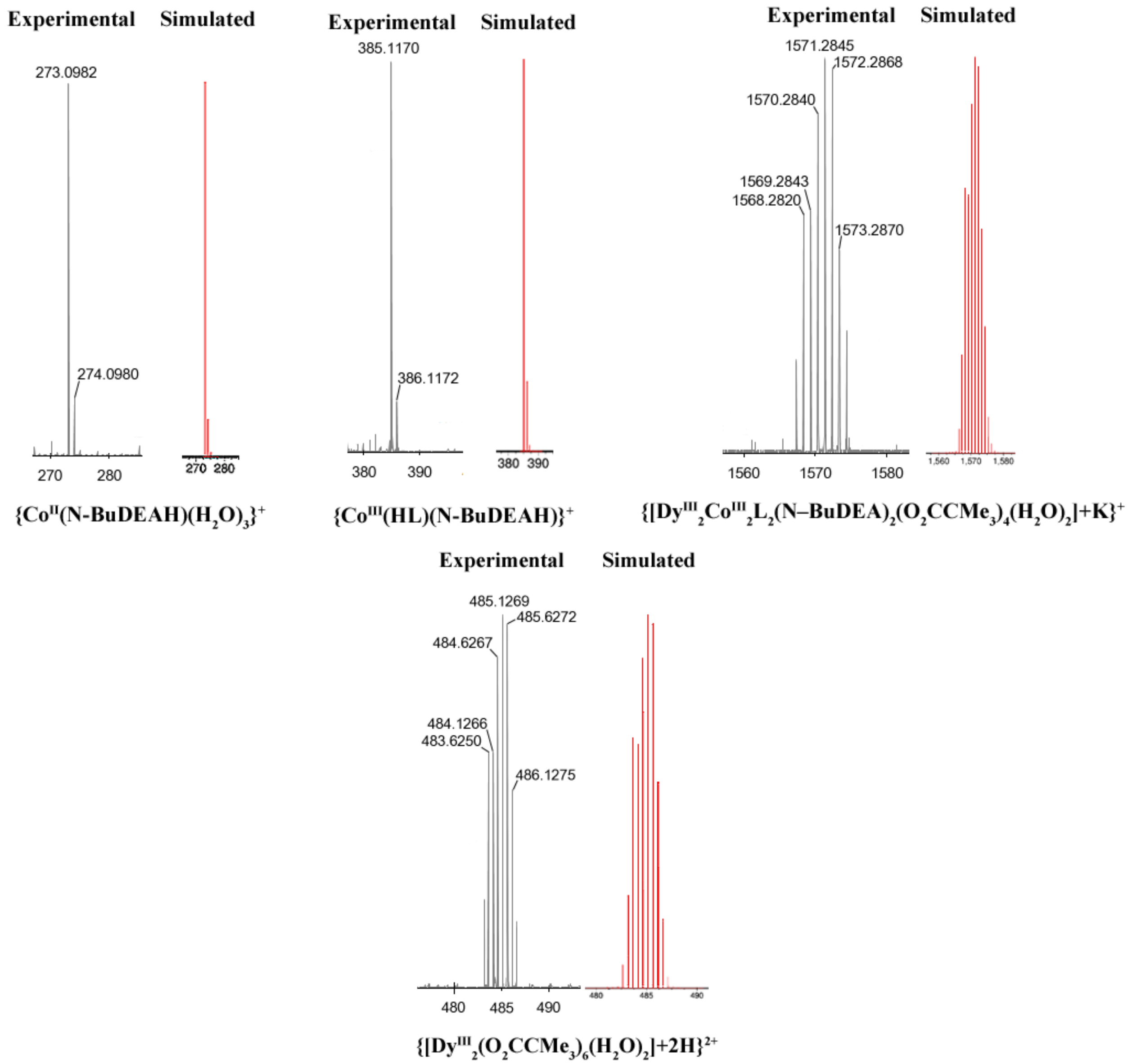

Fig. S13 Experimental and simulated peaks corresponding to different species present in solution obtained from HRMS (+ve) during synthesis of **3** in MeOH.

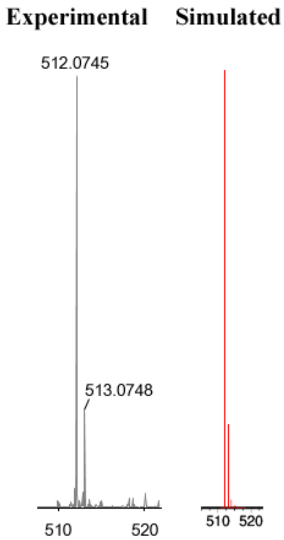

$\{Co^{II}_2(HL)(O_2CCMe_3)(MeOH)_4\}^+$

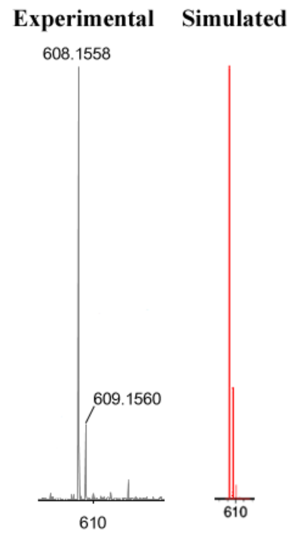

$\{Co^{II}Co^{III}L(N\text{-}BuDEAH)(O_2CCMe_3)(MeOH)_2\}^+$

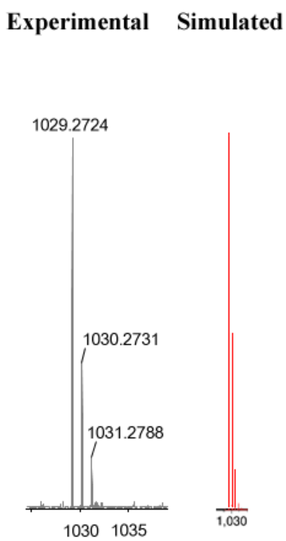

$\{Co^{II}Co^{III}_2L_2(N\text{–}BuDEAH)_2(O_2CCMe_3)_2\}^{\bullet+}$

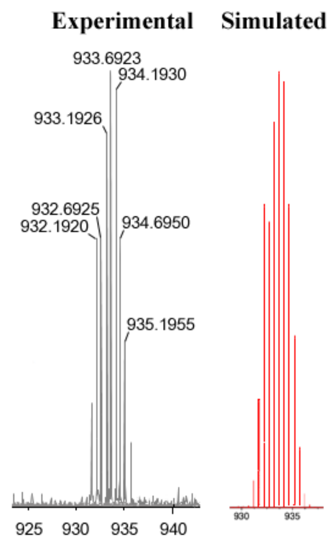

$\{[Dy^{III}_2Co^{II}Co^{III}_2L_2(N\text{–}BuDEA)_2(O_2CCMe_3)_6(MeOH)_2]+2Na\}^{2+}$

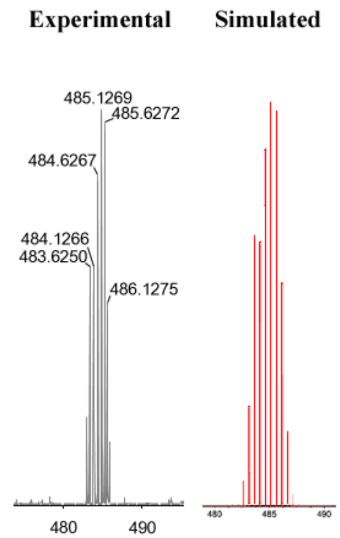

$\{[Dy^{III}_2(O_2CCMe_3)_6(H_2O)_2]+2H\}^{2+}$

Fig. S14 Experimental and simulated peaks corresponding to different species present in solution obtained from HRMS (+ve) during synthesis of **4** in MeOH.

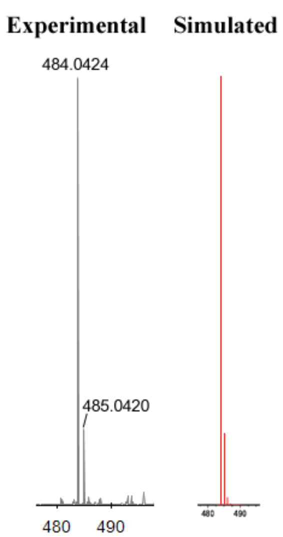

$\{Co^{II}_2L(O_2CCMe_3)(MeOH)_2(H_2O)_2\}^+$

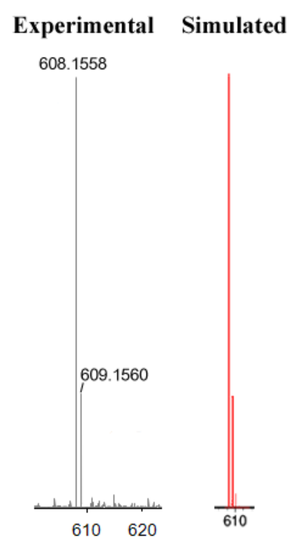

$\{Co^{II}Co^{III}L(N\text{-}BuDEAH)(O_2CCMe_3)(MeOH)_2\}^+$

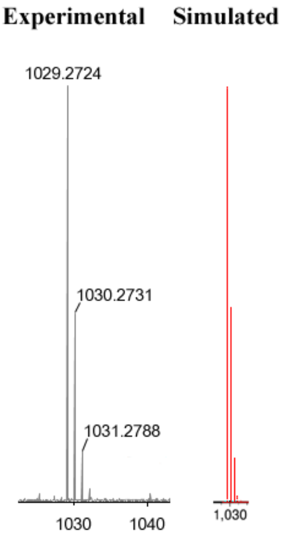

$\{Co^{II}Co^{III}_2L_2(N\text{–}BuDEAH)_2(O_2CCMe_3)_2\}^{\bullet+}$

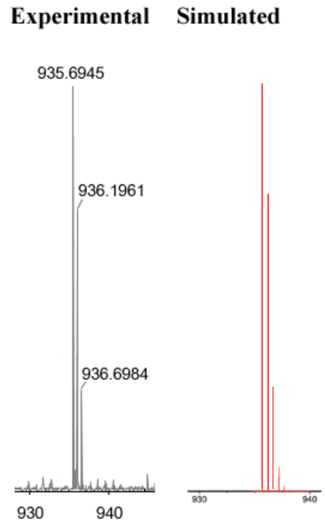

$\{[Ho^{III}_2Co^{II}Co^{III}_2L_2(N\text{–}BuDEA)_2(O_2CCMe_3)_6(MeOH)_2]+2Na\}^{2+}$

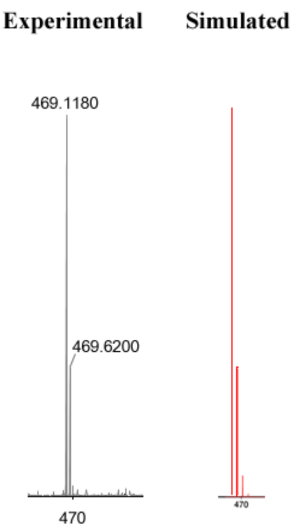

$\{[Ho^{III}_2(O_2CCMe_3)_6]+2H\}^{2+}$

Fig. S15 Experimental and simulated peaks corresponding to different species present in solution obtained from HRMS (+ve) for addition of H_2L before N−BuDEAH_2 during synthesis of **5** in MeOH.

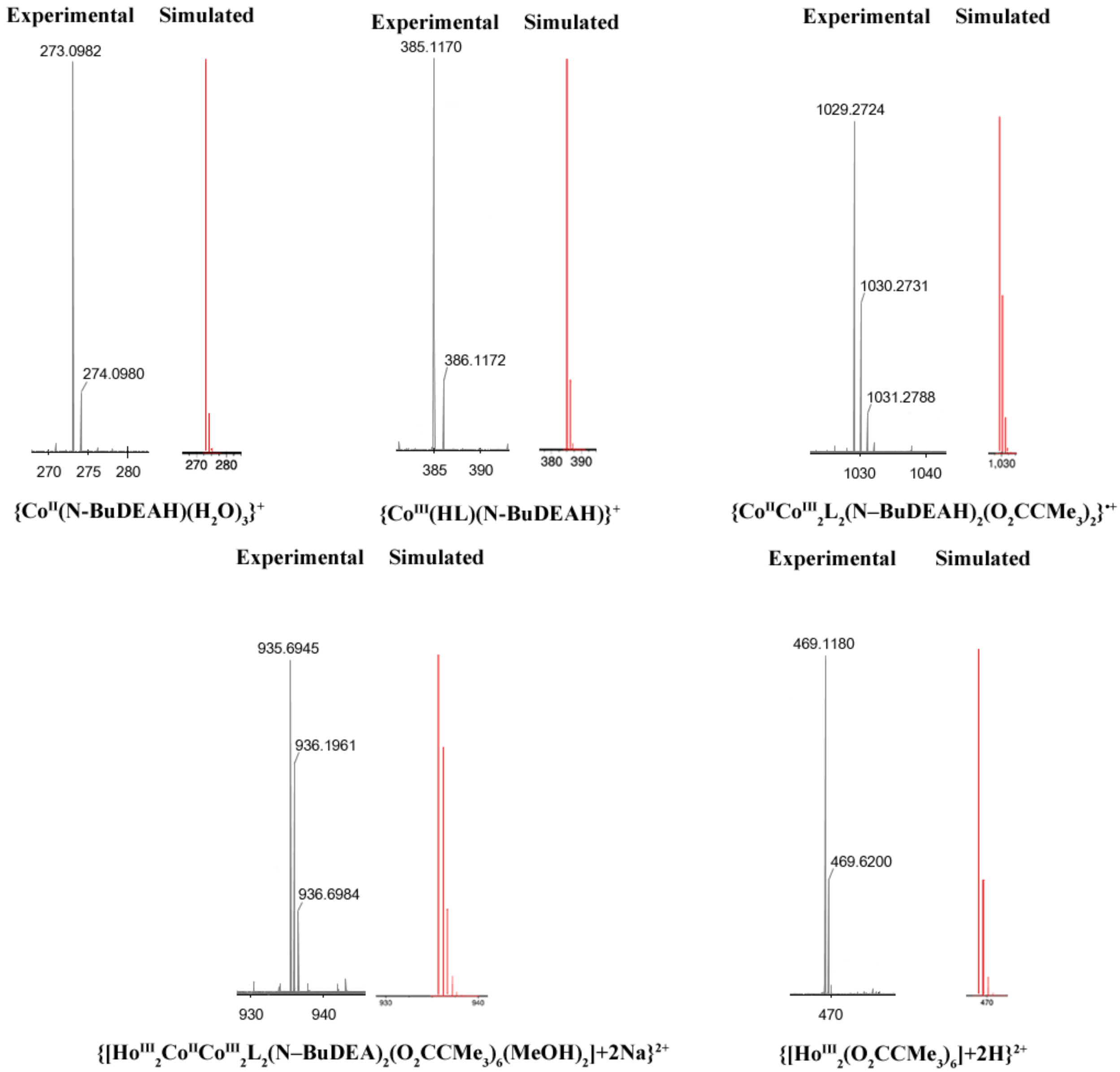

Fig. S16 Experimental and simulated peaks corresponding to different species present in solution obtained from HRMS (+ve) for addition of N−BuDEAH$_2$ before H$_2$L during synthesis of **5** in MeOH.

Aggregation pathways for 1, 2 and 5

In case of **1** and **2** when N–BuDEAH$_2$ was added before H$_2$L (Scheme S1; Path I), both the complexes showed peaks at *m*/*z* = 273.0982 and 385.1170 (Fig. S9 and S11) corresponding to {Co^{II}(N–BuDEAH)(H$_2$O)$_3$}$^+$ and {Co^{III}(HL)(N–BuDEA)}$^+$ (Scheme S1; species **a** and **b**) similar to **3**. Presence of dinuclear gadolinium and terbium pivalate, respectively, could also be ascertained from the peaks at *m*/*z* = 942.2235 (**1**, Fig. S9) and 1006.2750 (**2**, Fig. S11) corresponding to {Gd$^{III}{}_2$(O$_2$CCMe$_3$)$_6$(H$_2$O)}$^{\bullet+}$ ($C_{40}H_{56}Gd_2O_{13}$; calcd. 942.2232) and

$\{Tb^{III}{}_2(O_2CCMe_3)_6(MeOH)_2(H_2O)\}^{\bullet+}$ ($C_{40}H_{56}Gd_2O_{13}$; calcd. 942.2232). Peaks at m/z = 1524.3160 (Fig. S9) and 1524.3155 (Fig. S11) assignable to $\{[Gd^{III}{}_2Co^{III}{}_2L_2(N\text{–}BuDEA)_2(O_2CCMe_3)_4(H_2O)_2]\}^{\bullet+}$ ($C_{52}H_{88}Co_2Gd_2N_4O_{20}$; calcd. 1524.3167) and $\{[Tb^{III}{}_2Co^{III}{}_2L_2(N\text{–}BuDEA)_2(O_2CCMe_3)_4(H_2O)_2]\}^{\bullet+}$ ($C_{52}H_{88}Co_2Tb_2N_4O_{20}$; calcd. 1524.3163) respectively confirmed the existence of **1** and **2** in solution.

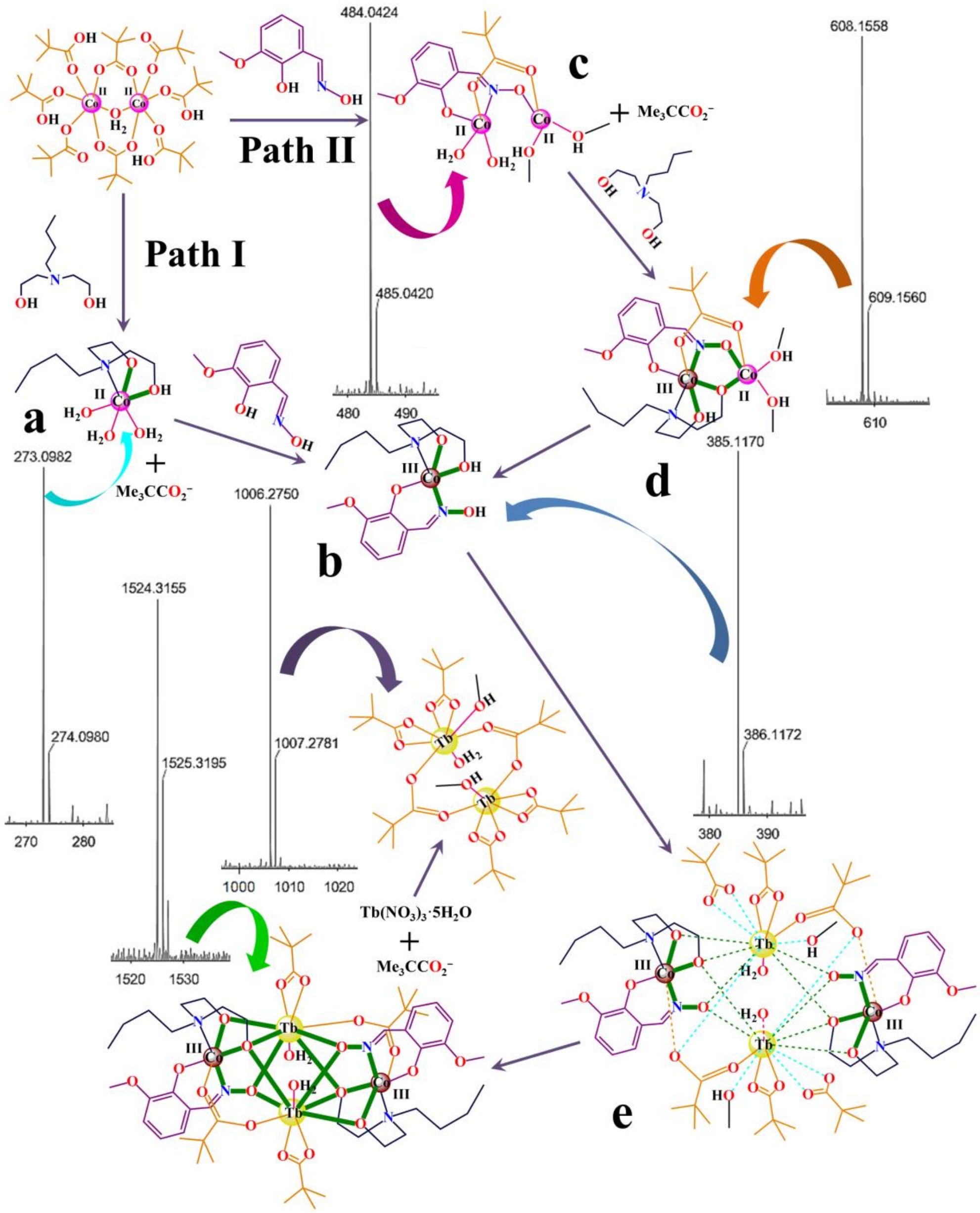

Scheme S1 Proposed pathway for the formation of **2** in MeOH medium for different order of addition of H_2L and N–BuDEAH_2. **1** exhibits a very similar pathway for aggregation reaction.

When H_2L is added before N–BuDEAH$_2$ (Scheme S1, Path II), the complexes show peaks at *m*/*z* = 484.0424 and 608.1558 (Fig. S10 and S12) corresponding to dinuclear species $\{Co^{II}_2(HL)(O_2CCMe_3)(MeOH)_2(H_2O)_2\}^+$ ($C_{15}H_{28}Co_2NO_9$; calcd. 484.0428) and $\{Co^{II}Co^{III}L$(N–BuDEAH)$(O_2CCMe_3)(MeOH)_2\}^+$ (Scheme S1; species **c** and **d**) similar to **4**. Unlike **4**, the mass spectra also shows a peak at *m*/*z* = 385.1170 for the species $\{Co^{III}(HL)$(N–BuDEA)$\}^+$ (Scheme S1; species **b**) as observed when N–BuDEAH$_2$ is added first. The presence of lanthanide pivalates and complexes **1** and **2** in solution could be ascertained from peaks similar to those described earlier.

In case of **5**, for addition of H_2L first (Scheme S2, Path I), the presence of dinuclear species $\{Co^{II}_2(HL)(O_2CCMe_3)(MeOH)_2(H_2O)_2\}^+$ and $\{Co^{II}Co^{III}L$(N–BuDEAH)$(O_2CCMe_3)(MeOH)_2\}^+$ (Scheme S2; species **c** and **d**) are ascertained from peaks at *m*/*z* = 484.0424 and 608.1558 (Fig. S15) while the peak at *m*/*z* = 1029.2724 is due to the trinuclear species $\{Co^{II}Co^{III}_2L_2$(N–BuDEAH)$_2(O_2CCMe_3)_2\}^{\bullet+}$ (Scheme S2; species **e**). Dinuclear holmium pivalate could be identified from the peak at *m*/*z* = 469.1180 corresponding to $\{[Ho^{III}_2(O_2CCMe_3)_6]+2H\}^{2+}$ ($C_{30}H_{56}Ho_2O_{12}$; calcd. 469.1184) which is trapped by species **e** forming complex **5** via intermediate **f** (Scheme S2). The species $\{[Ho^{III}_2Co^{II}Co^{III}_2L_2$(N–BuDEA)$_2(O_2CCMe_3)_6(MeOH)_2]+2Na\}^{2+}$ ($C_{64}H_{110}Co_3Ho_2N_4Na_2O_{24}$; calcd. 935.6949) identified from the peak at *m*/*z* = 935.6945 points to the presence of **5** in solution. When N–BuDEAH$_2$ is added before H_2L (Scheme S2; Path II), mononuclear species $\{Co^{II}$(N–BuDEAH)$(H_2O)_3\}^+$ and $\{Co^{III}(HL)$(N–BuDEA)$\}^+$ (Scheme S2; species **a** and **b**) could be identified at *m*/*z* = 273.0982 and 385.1170 (Fig. S16) similar to **3**. But unlike **3**, the trinuclear species $\{Co^{II}Co^{III}_2L_2$(N–BuDEAH)$_2(O_2CCMe_3)_2\}^{\bullet+}$ (Scheme S2; species **e**) was identified from the peak at *m*/*z* = 1029.2724, formed by the trapping of a Co^{II} ion along with two $Me_3CCO_2^-$ anions by two species **b**. This process is perhaps less favourable resulting in lower yields of **5** by Path II. The presence of dinuclear holmium pivalate and complex **5** in solution were ascertained as described earlier. Formation of **5** from species **e** through intermediate **f** is similar to that described previously (Scheme S2).

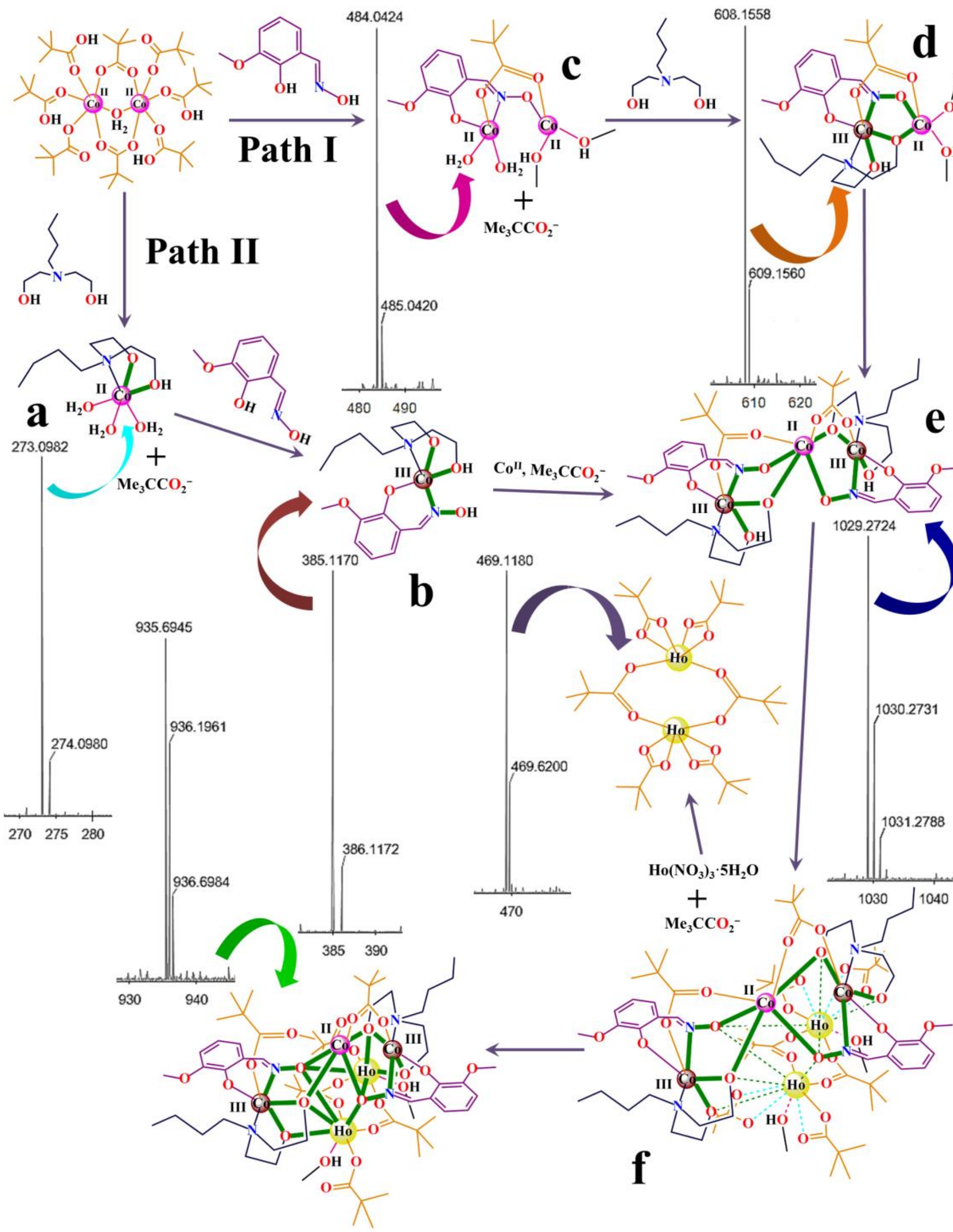

Scheme S2 Proposed pathway for the formation of **5** in MeOH medium for different order of addition of H_2L and N−BuDEAH$_2$.

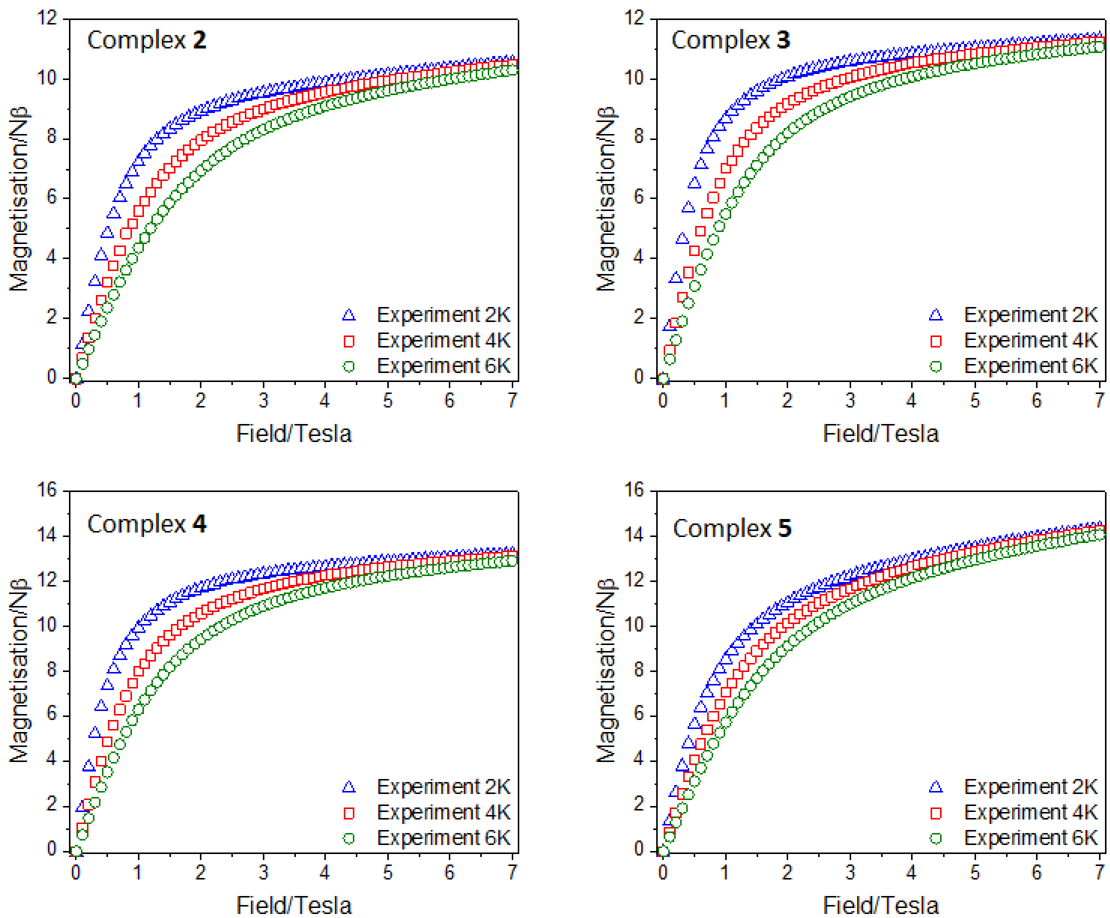

Fig. S17 Magnetization *vs.* field data at 2, 4 and 6 K for complexes **2–5**.

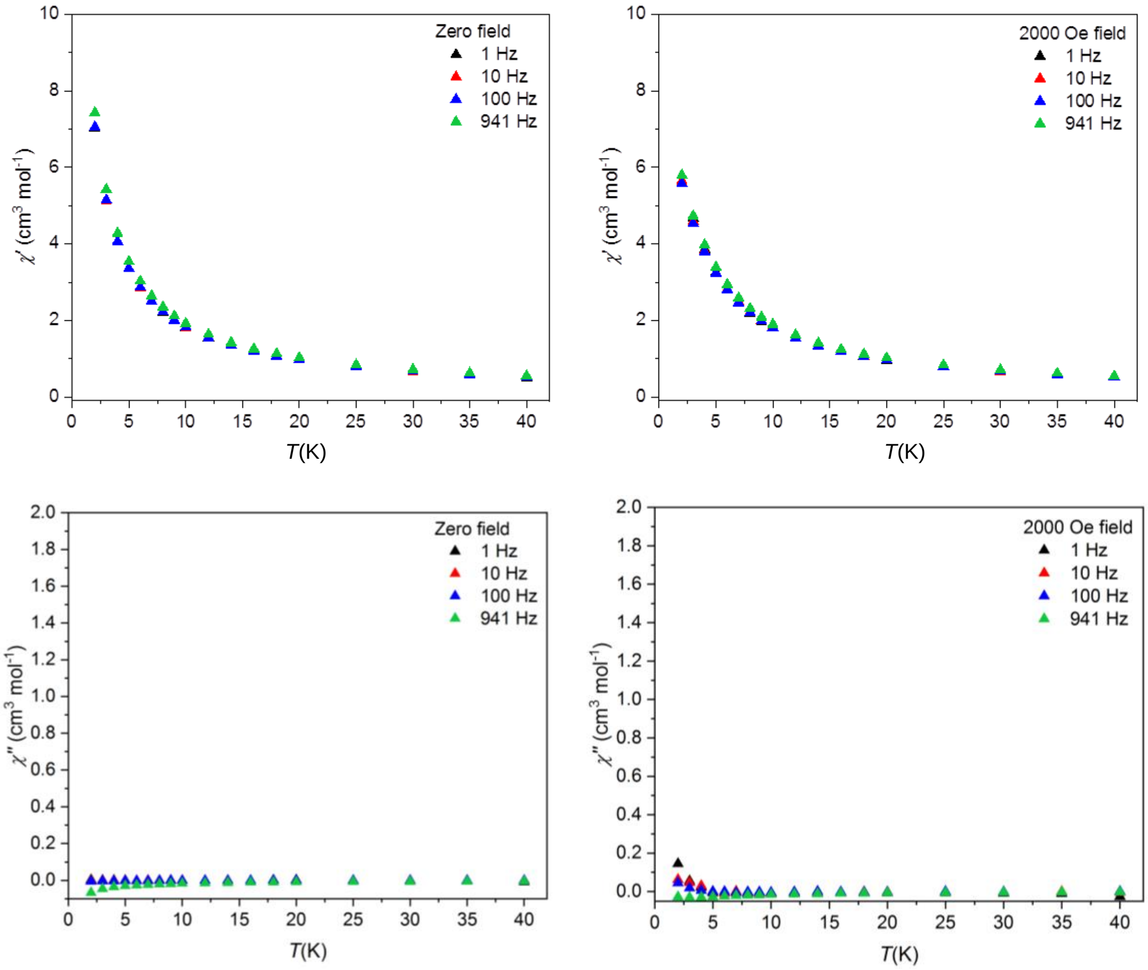

Fig. S18 The in-phase (χ') and out-of-phase (χ'') ac susceptibility data for complex **2** in zero dc field (left) and 2000 Oe dc applied field (right).

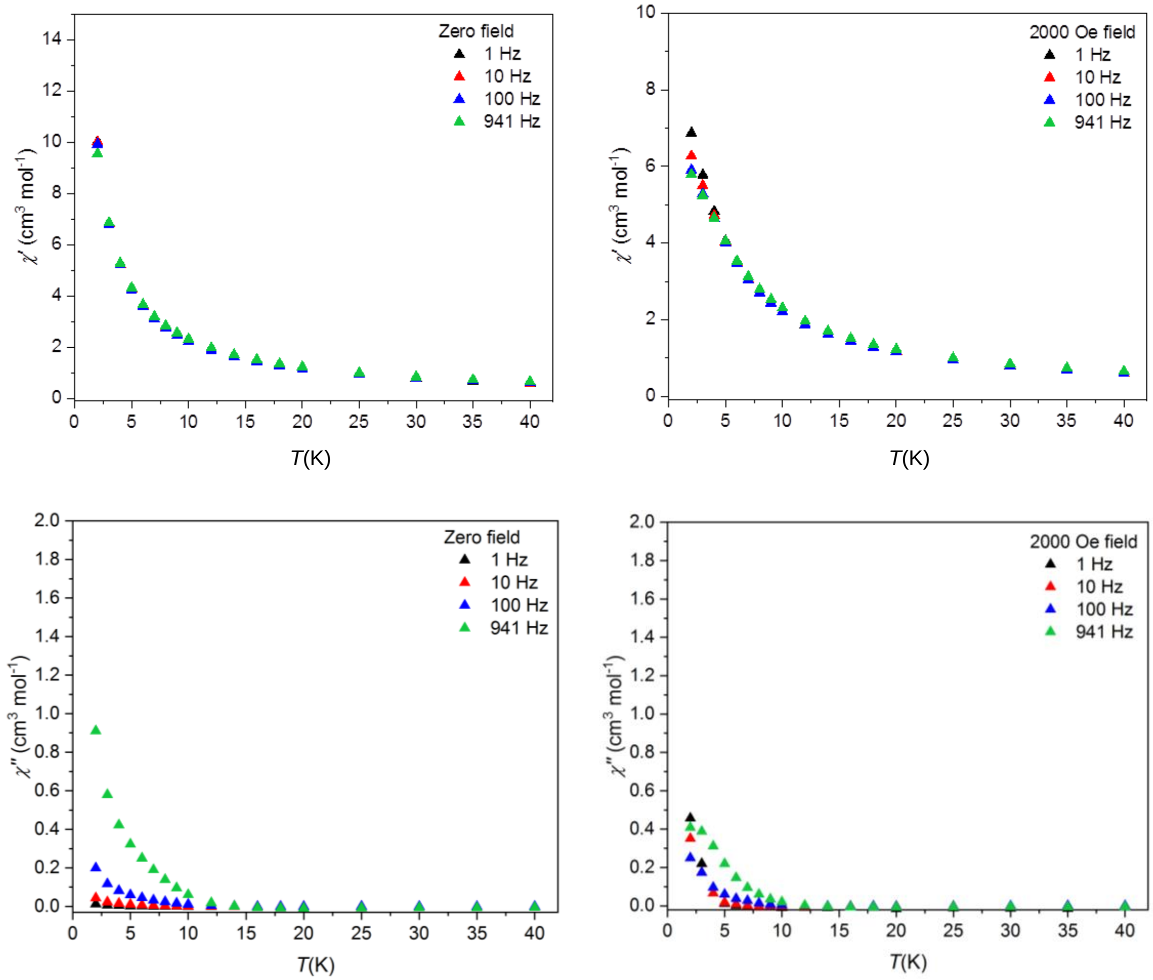

Fig. S19 The in-phase (χ') and out-of-phase (χ'') ac susceptibility data for complex **3** in zero dc field (left) and 2000 Oe dc applied field (right).

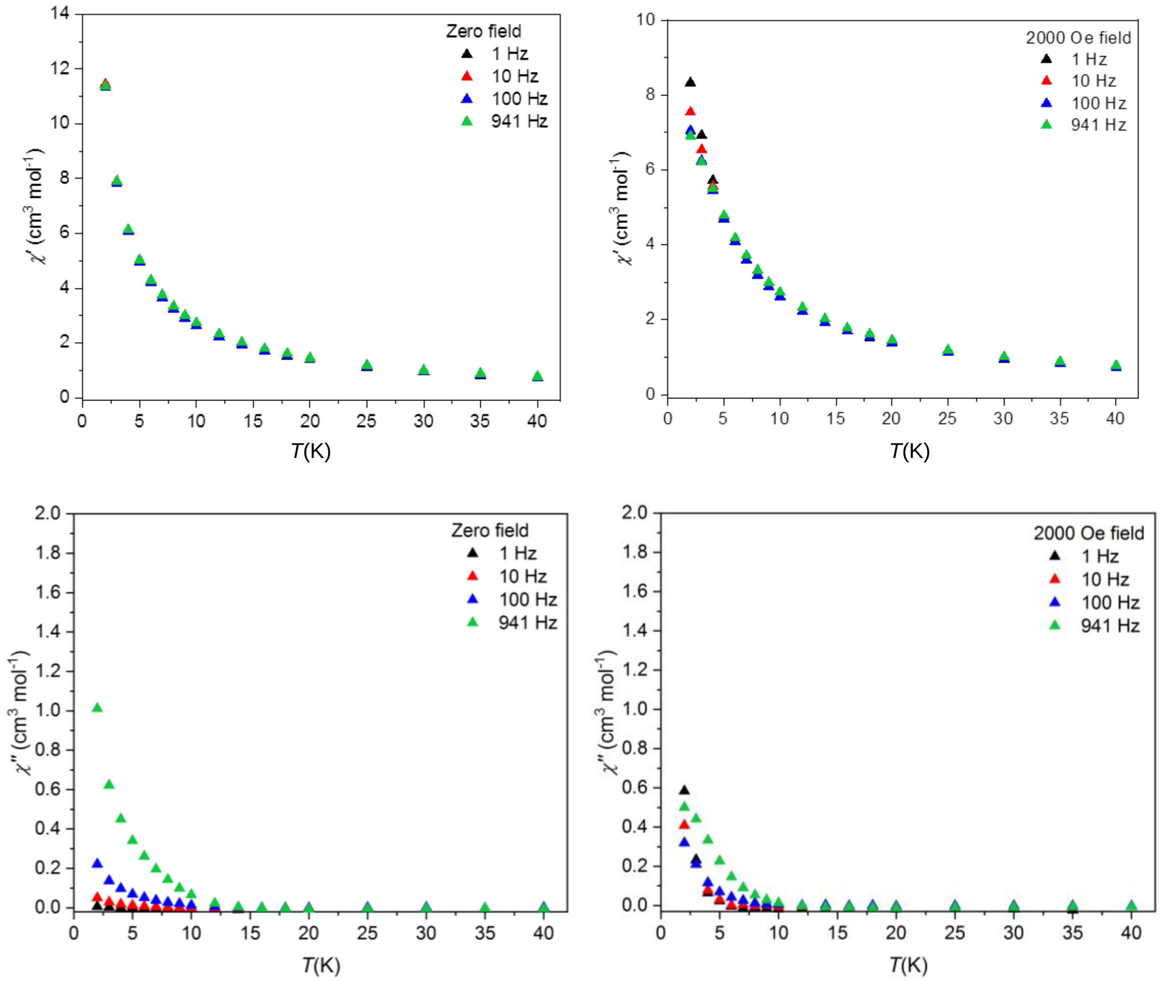

Fig. S20 The in-phase (χ') and out-of-phase (χ'') ac susceptibility data for complex **4** in zero dc field (left) and 2000 Oe dc applied field (right).

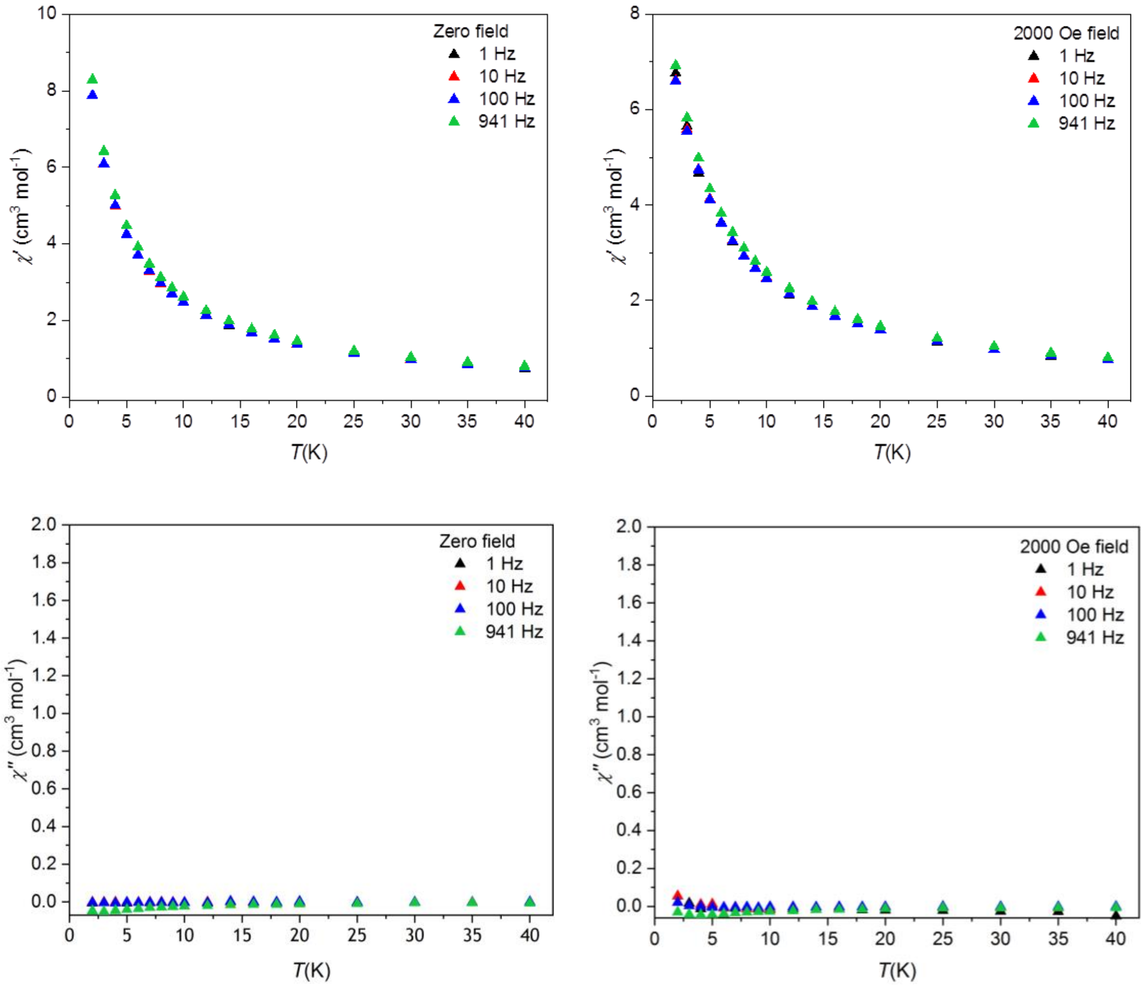

Fig. S21 The in-phase (χ') and out-of-phase (χ'') ac susceptibility data for complex **5** in zero dc field (left) and 2000 Oe dc applied field (right).

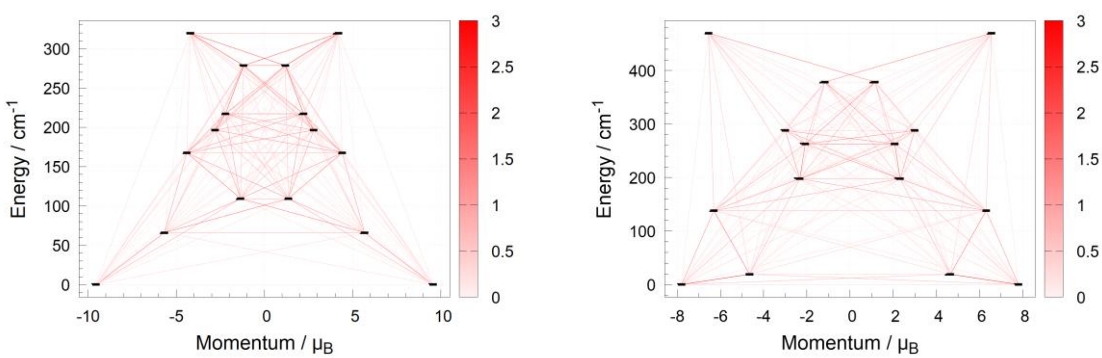

Fig. S22 Magnetization blocking barrier of Dy^{III} in **3** (left) and **4** (right) calculated by SINGLE_ANISO, where magnetic relaxation path, outlining the blocking barrier, is traced by the white-red lines scaling the transition magnetic dipole matrix elements between the connected multiplet states.

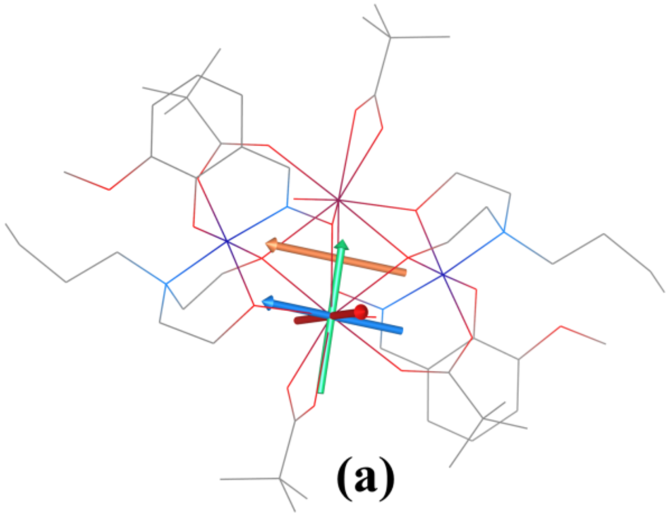

Fig. S23 The molecular structure of **3** (a) and simplified structure of **4** (b) derived from the experimental X-ray geometry used for CASSCF calculations overlaid with principal axis of *g*-tensor of the first Kramers doublet (x/y/z-axes colored as red/green/blue arrows) for Dy^{III} and Co^{II} ions resulting from SINGLE_ANISO. Note: (a) the first Kramers doublet of Dy^{III} has $g_x = 0.158$, $g_y = 0.424$, $g_z = 19.117$, (b) the first Kramers doublet of Dy^{III} has $g_x = 0.359$, $g_y = 2.296$, $g_z = 15.611$, the first Kramers doublet of Co^{II} has $g_x = 2.232$, $g_y = 2.853$, $g_z = 7.405$ ($S_{eff} = 1/2$).

The orange arrows situated in the center of the complexes represents orientation of g_z of the (a) second doublet and (b) first Kramers doublet resulting from POLY_ANISO calculations (Fig. 9 and 10). Note: (a) the first doublet has $g_x = g_y = g_z = 0.0$, the second doublet has $g_x = g_y = 0.0$ and $g_z = 38.2$, (b) the first doublet has $g_x = 0.035$, $g_y = 3.217$, $g_z = 11.724$.

2

$J^{\mathrm{exch}}_{\mathrm{Tb-Tb}} = +0.0020\ \mathrm{cm}^{-1}$

Scaling factor for calculated data: 0.957

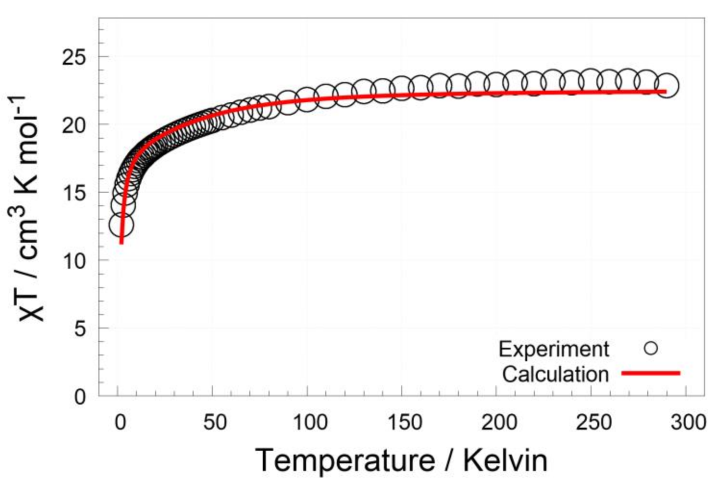

3

$J^{\mathrm{exch}}_{\mathrm{Dy-Dy}}$ = +0.122 cm^{-1}

Scaling factor for

calculated data: 0.953

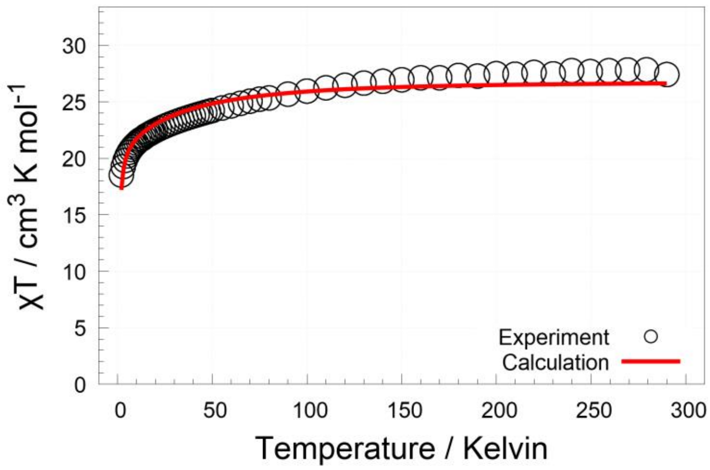

4

$J^{\mathrm{exch}}_{\mathrm{Co-Dy}}$ = +3.18 cm^{-1}

$J^{\mathrm{exch}}_{\mathrm{Dy-Dy}}$ = –1.602 cm^{-1}

Scaling factor for

calculated data: 1.037

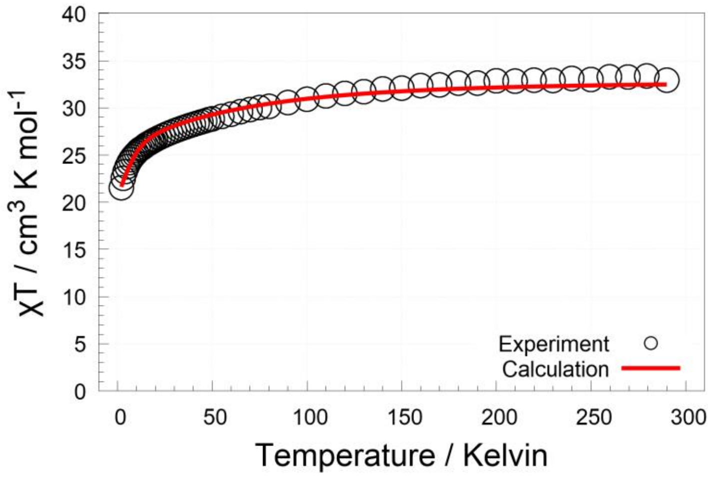

5

$J^{\mathrm{exch}}_{\mathrm{Co-Ho}}$ = –0.390 cm^{-1}

$J^{\mathrm{exch}}_{\mathrm{Ho-Ho}}$ = –0.020 cm^{-1}

Scaling factor for

calculated data: 1.090

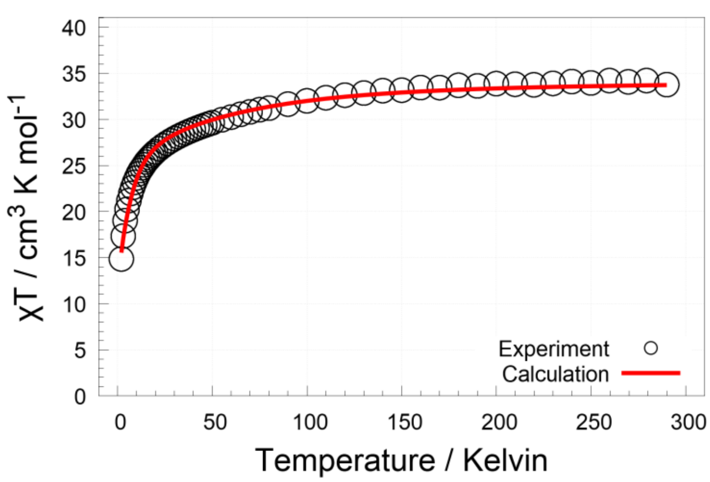

Fig. S24 The fits of experimental magnetic susceptibility of **2–5** utilizing POLY_ANISO module.

Table S1 Important bond lengths (Å) and angles (°) in **1–5**

Bond lengths (Å)					
Complex **1**					
Gd1–O7	2.361(4)	Gd1–O9	2.492(4)	Co1–O4	1.904(3)
Gd1–O5	2.407(4)	Gd1–O4	2.539(3)	Co1–O5	1.907(3)
Gd1–O1W	2.423(3)	Gd1–O4	2.558(4)	Co1–N2	1.990(4)
Gd1–O3	2.429(3)	Co1–N1	1.870(4)	Gd1–Co1	3.356(2)
Gd1–O3	2.438(3)	Co1–O1	1.887(3)	Gd1–Co1	3.809(29)
Gd1–O8	2.453(3)	Co1–O6	1.904(4)	Gd1–Gd1	3.4356(17)
Complex **2**					
Tb1–O7	2.324(7)	Tb1–O9	2.496(7)	Co1–O5	1.913(7)
Tb1–O5	2.381(8)	Tb1–O4	2.533(7)	Co1–O6	1.913(7)
Tb1–O1W	2.386(7)	Tb1–O4	2.541(7)	Co1–N2	1.987(9)
Tb1–O8	2.401(7)	Co1–N1	1.855(8)	Tb1–Co1	3.338(3)
Tb1–O3	2.418(7)	Co1–O1	1.883(8)	Tb1–Co1	3.803(3)
Tb1–O3	2.431(7)	Co1–O4	1.891(7)	Tb1–Tb1	3.436(2)
Complex **3**					
Dy1–O7	2.319(3)	Dy1–O9	2.477(3)	Co1–O4	1.899(3)
Dy1–O5	2.358(3)	Dy1–O4	2.509(3)	Co1–O6	1.900(3)
Dy1–O1W	2.377(3)	Dy1–O4	2.535(3)	Co1–N2	1.985(3)
Dy1–O3	2.403(3)	Co1–N1	1.862(3)	Dy1–Co1	3.3166(5)
Dy1–O3	2.411(3)	Co1–O1	1.887(3)	Dy1–Co1	3.7860(1)
Dy1–O8	2.441(3)	Co1–O5	1.897(3)	Dy1–Dy1	3.3962(4)
Complex **4**					
Dy1–O8	2.260(6)	Co2–O6	2.025(7)	Co1–O4	2.005(7)
Dy1–O5	2.306(6)	Co2–O4	2.049(5)	Co1–Co2	3.2910(11)
Dy1–O10	2.309(6)	Co2–O3	2.102(5)	Dy1–Co1	3.3002(14)
Dy1–O9	2.352(5)	Co1–O1	1.881(7)	Dy1–Co1	5.1624(13)
Dy1–O12	2.365(5)	Co1–O5	1.880(6)	Dy1–Co2	3.3775(15)

Dy1–O3	2.422(5)	Co1–N1	1.893(6)	Dy1–Dy1	3.8129(15)
Dy1–O4	2.537(5)	Co1–O7	1.917(6)		
Dy1–O3	2.583(5)	Co1–N2B	2.004(17)		
Complex **5**					
Ho1 – O8	2.241(7)	Co2–O6	2.007(8)	Co1–N2B	2.01(3)
Ho1 – O10	2.282(7)	Co2–O4	2.047(5)	Co1–Co2	3.2745(6)
Ho1 – O5	2.284(6)	Co2–O3	2.089(6)	Ho1–Co1	5.1370(7)
Ho1 – O9	2.333(6)	Co1 – O1	1.872(7)	Ho1–Co1	3.2729(14)
Ho1 – O12	2.347(6)	Co1 – O5	1.877(6)	Ho1–Co2	3.3623(14)
Ho1 – O3	2.403(6)	Co1 – N1	1.882(7)	Ho1–Ho1	3.7887(10)
Ho1 – O4	2.527(5)	Co1 – O7	1.907(7)		
Ho1 – O3	2.553(6)	Co1 – O4	1.985(7)		
Bond angles (°)					
Complex **1**					
O7–Gd1–O5	146.68(12)	O3–Gd1–O9	143.54(11)	O1–Co1–O6	88.33(15)
O7–Gd1–O1W	79.31(12)	O8–Gd1–O9	52.71(11)	N1–Co1–O4	89.79(16)
O5–Gd1–O1W	86.47(12)	O7–Gd1–O4	142.83(11)	O1–Co1–O4	178.37(15)
O7–Gd1–O3	83.35(12)	O5–Gd1–O4	64.04(11)	O6–Co1–O4	93.29(14)
O5–Gd1–O3	123.01(12)	O1W–Gd1–O4	134.94(11)	N1–Co1–O5	89.28(16)
O1–Gd1–O3	144.14(12)	O3–Gd1–O4	60.32(10)	O1–Co1–O5	91.29(15)
O7–Gd1–O3	129.34(12)	O3–Gd1–O4	63.12(11)	O6–Co1–O5	177.71(15)
O5–Gd1–O3	75.15(11)	O8–Gd1–O4	85.04(11)	O4–Co1–O5	87.08(14)
O1–Gd1–O3	77.33(12)	O9–Gd1–O4	123.59(12)	N1–Co1–N2	175.13(17)
O3–Gd1–O3	90.20(11)	O7–Gd1–O4	72.73(12)	O1–Co1–N2	91.13(17)
O7–Gd1–O8	78.32(12)	O5–Gd1–O4	135.03(11)	O6–Co1–N2	91.73(16)
O5–Gd1–O8	88.23(12)	O1W–Gd1–O4	81.92(12)	O4–Co1–N2	88.73(16)
O1–Gd1–O8	129.61(12)	O3–Gd1–O4	62.95(11)	O5–Co1–N2	86.02(16)
O3–Gd1–O8	75.97(12)	O3–Gd1–O4	59.94(11)	Co1–O5–Gd1	101.52(14)
O3–Gd1–O8	147.96(11)	O8–Gd1–O4	131.56(11)	Gd1–O3–Gd1	89.80(11)

O7–Gd1–O9	69.97(13)	O9–Gd1–O4	139.89(11)	Co1–O4–Gd1	97.05(13)
O5–Gd1–O9	77.59(12)	O4–Gd1–O4	95.25(10)	Co1–O4–Gd1	116.45(15)
O1W–Gd1–O9	77.26(12)	N1–Co1–O1	90.22(17)	Gd1–O4–Gd1	84.75(10)
O3–Gd1–O9	125.20(11)	N1–Co1–O6	92.98(16)		
Complex **2**					
O7–Tb1–O5	146.1(3)	O3–Tb1–O9	126.0(2)	O1–Co1–O4	178.5(3)
O7–Tb1–O1W	78.8(3)	O3–Tb1–O9	143.3(2)	N1–Co1–O5	89.1(3)
O5–Tb1–O1W	86.3(3)	O7–Tb1–O4	143.2(2)	O1–Co1–O5	91.2(3)
O7–Tb1–O8	77.8(3)	O5–Tb1–O4	64.6(2)	O4–Co1–O5	87.4(3)
O5–Tb1–O8	88.7(3)	O1W–Tb1–O4	134.9(2)	N1–Co1–O6	93.2(3)
O1W–Tb1–O8	128.9(2)	O8–Tb1–O4	86.2(2)	O1–Co1–O6	89.0(3)
O7–Tb1–O3	83.8(2)	O3–Tb1–O4	60.2(2)	O4–Co1–O6	92.4(3)
O5–Tb1–O3	123.4(2)	O3–Tb1–O4	62.6(2)	O5–Co1–O6	177.7(3)
O1W–Tb1–O3	144.0(3)	O9–Tb1–O4	124.4(2)	N1–Co1–N2	175.2(3)
O8–Tb1–O3	76.3(2)	O7–Tb1–O4	72.7(3)	O1–Co1–N2	90.4(4)
O7–Tb1–O3	129.2(3)	O5–Tb1–O4	135.4(2)	O4–Co1–N2	89.9(3)
O5–Tb1–O3	75.5(3)	O1W–Tb1–O4	82.2(2)	O5–Co1–N2	86.3(3)
O1W–Tb1–O3	77.7(2)	O8–Tb1–O4	131.1(3)	O6–Co1–N2	91.4(3)
O8–Tb1–O3	148.6(2)	O3–Tb1–O4	62.6(2)	Co1–O5–Tb1	101.5(3)
O3–Tb1–O3	89.8(2)	O3–Tb1–O4	59.9(2)	Tb1–O3–Tb1	90.2(2)
O7–Tb1–O9	69.8(3)	O9–Tb1–O4	139.7(2)	Co1–O4–Tb1	96.9(3)
O5–Tb1–O9	77.1(3)	O4–Tb1–O4	94.8(2)	Co1–O4–Tb1	117.4(3)
O1W–Tb1–O9	76.5(2)	N1–Co1–O1	90.8(4)	Tb1–O4–Tb1	85.2(2)
O8–Tb1–O9	52.9(2)	N1–Co1–O4	88.7(3)		
Complex **3**					
O7–Dy1–O5	145.97(10)	O3–Dy1–O9	143.04(10)	O1–Co1–O5	91.20(12)
O7–Dy1–O1W	79.57(10)	O8–Dy1–O9	52.86(10)	N1–Co1–O4	90.06(13)
O5–Dy1–O1W	85.69(10)	O7–Dy1–O4	143.12(10)	O1–Co1–O4	177.66(13)
O7–Dy1–O3	83.61(10)	O5–Dy1–O4	64.49(9)	O5–Co1–O4	86.47(12)

O5–Dy1–O3	123.36(10)	O1W–Dy1–O4	134.48(9)	N1–Co1–O6	92.52(13)
O1W–Dy1–O3	144.65(10)	O3–Dy1–O4	60.32(9)	O1–Co1–O6	89.17(12)
O7–Dy1–O3	129.03(10)	O3–Dy1–O4	63.30(9)	O5–Co1–O6	177.89(12)
O5–Dy1–O3	75.80(9)	O8–Dy1–O4	85.44(9)	O4–Co1–O6	93.17(12)
O1W–Dy1–O3	77.00(10)	O9–Dy1–O4	123.74(10)	N1–Co1–N2	174.93(14)
O3–Dy1–O3	90.24(9)	O7–Dy1–O4	72.64(9)	O1–Co1–N2	91.30(14)
O7–Dy1–O8	78.23(10)	O5–Dy1–O4	135.58(9)	O5–Co1–N2	85.45(13)
O5–Dy1–O8	88.02(9)	O1W–Dy1–O4	82.28(10)	O4–Co1–N2	88.78(13)
O1W–Dy1–O8	129.22(10)	O3–Dy1–O4	63.02(9)	O6–Co1–N2	92.47(13)
O3–Dy1–O8	76.21(10)	O3–Dy1–O4	59.85(9)	Co1–O5–Dy1	101.87(12)
O3–Dy1–O8	148.53(10)	O8–Dy1–O4	131.60(9)	Dy1–O3–Dy1	89.76(9)
O7–Dy1–O9	70.10(10)	O9–Dy1–O4	139.80(9)	Co1–O4–Dy1	96.64(12)
O5–Dy1–O9	76.75(9)	O4–Dy1–O4	95.34(8)	Co1–O4–Dy1	116.57(12)
O1W–Dy1–O9	76.71(10)	N1–Co1–O1	89.65(14)	Dy1–O4–Dy1	84.66(8)
O3–Dy1–O9	125.72(9)	N1–Co1–O5	89.56(13)		
Complex **4**					
O8–Dy1–O5	84.7(2)	O3–Dy1–O4	71.46(18)	O5–Co1–O7	177.1(2)
O8–Dy1–O10	154.64(19)	O8–Dy1–O3	71.98(17)	O1–Co1–O7	88.3(3)
O5–Dy1–O10	103.0(2)	O5–Dy1–O3	80.30(19)	N1–Co1–O7	91.5(3)
O8–Dy1–O9	79.5(2)	O10–Dy1–O3	132.81(18)	O5–Co1–N2B	91.0(6)
O5–Dy1–O9	153.8(2)	O9–Dy1–O3	113.76(18)	O1–Co1–N2B	98.1(6)
O10–Dy1–O9	83.9(2)	O12–Dy1–O3	147.4(2)	N1–Co1–N2B	169.7(6)
O8–Dy1–O12	81.4(2)	O3–Dy1–O3	58.1(2)	O7–Co1–N2B	86.1(6)
O5–Dy1–O12	78.82(19)	O4–Dy1–O3	61.02(14)	O5–Co1–O4	84.6(3)
O10–Dy1–O12	76.6(2)	O6–Co2–O6	98.1(4)	O1–Co1–O4	175.2(2)
O9–Dy1–O12	78.29(18)	O6–Co2–O4	95.6(3)	N1–Co1–O4	91.8(3)
O8–Dy1–O3	104.16(18)	O6–Co2–O4	95.5(3)	O7–Co1–O4	94.8(3)
O5–Dy1–O3	130.57(19)	O4–Co2–O4	163.0(3)	N2B–Co1–O4	78.5(5)
O10–Dy1–O3	89.3(2)	O6–Co2–O3	165.0(2)	Co1–O4–Co2	108.5(2)

O9–Dy1–O3	74.03(17)	O6–Co2–O3	95.9(2)	Co1–O4–Dy1	92.5(2)
O12–Dy1–O3	150.08(19)	O4–Co2–O3	77.5(2)	Co2–O4–Dy1	94.26(18)
O8–Dy1–O4	126.90(18)	O4–Co2–O3	88.5(2)	Co2–O3–Dy1	96.3(2)
O5–Dy1–O4	65.2(2)	O3–Co2–O3	70.8(3)	Co2–O3–Dy1	91.69(19)
O10–Dy1–O4	77.55(17)	O5–Co1–O1	92.1(3)	Dy1–O3–Dy1	99.2(2)
O9–Dy1–O4	140.7(2)	O5–Co1–N1	91.4(3)	Co1–O5–Dy1	103.6(3)
O12–Dy1–O4	128.81(18)	O1–Co1–N1	91.8(3)		
Complex **5**					
O8–Ho1–O10	154.5(2)	O3–Ho1–O4	71.63(19)	O1–Co1–O7	88.5(3)
O8–Ho1–O5	84.8(2)	O8–Ho1–O3	72.23(19)	O5–Co1–O7	177.5(3)
O10–Ho1–O5	103.0(2)	O10–Ho1–O3	132.6(2)	N1–Co1–O7	91.5(3)
O8–Ho1–O9	79.1(2)	O5–Ho1–O3	80.9(2)	O1–Co1–O4	175.3(2)
O10–Ho1–O9	83.9(2)	O9–Ho1–O3	113.6(2)	O5–Co1–O4	84.9(3)
O5–Ho1–O9	153.3(2)	O12–Ho1–O3	147.7(2)	N1–Co1–O4	91.6(3)
O8–Ho1–O12	81.3(2)	O3–Ho1–O3	57.5(3)	O7–Co1–O4	94.5(3)
O10–Ho1–O12	76.7(2)	O4–Ho1–O3	61.28(16)	O1–Co1–N2B	96.9(8)
O5–Ho1–O12	78.5(2)	O6–Co2–O6	98.0(4)	O5–Co1–N2B	91.7(9)
O9–Ho1–O12	78.1(2)	O6–Co2–O4	95.5(3)	N1–Co1–N2B	170.8(8)
O8–Ho1–O3	103.8(2)	O6–Co2–O4	95.6(3)	O7–Co1–N2B	85.7(9)
O10–Ho1–O3	89.5(2)	O4–Co2–O4	163.0(3)	O4–Co1–N2B	79.9(8)
O5–Ho1–O3	130.8(2)	O6–Co2–O3	164.4(3)	Co1–O4–Co2	108.6(2)
O9–Ho1–O3	74.23(19)	O6–Co2–O3	96.5(3)	Co1–O4–Ho1	92.2(2)
O12–Ho1–O3	150.2(2)	O4–Co2–O3	88.5(2)	Co2–O4–Ho1	94.03(19)
O8–Ho1–O4	127.3(2)	O4–Co2–O3	77.5(2)	Co2–O3–Ho1	96.7(3)
O10–Ho1–O4	77.30(19)	O3–Co2–O3	69.7(4)	Co2–O3–Ho1	92.3(2)
O5–Ho1–O4	65.4(2)	O1–Co1–O5	91.9(3)	Ho1–O3–Ho1	99.7(2)
O9–Ho1–O4	140.9(2)	O1–Co1–N1	91.9(3)	Co1–O5–Ho1	103.3(3)
O12–Ho1–O4	128.65(19)	O5–Co1–N1	90.9(3)		

Table S2 Continuous Shape Measures calculation for Ln^{III} in **1–5**

S H A P E v2.1 Continuous Shape Measures calculation
(c) 2013 Electronic Structure Group, Universitat de Barcelona
Contact: llunell@ub.edu

[ML_9]

EP-9	1 D9h	Enneagon
OPY-9	2 C8v	Octagonal pyramid
HBPY-9	3 D7h	Heptagonal bipyramid
JTC-9	4 C3v	Johnson triangular cupola J3
JCCU-9	5 C4v	Capped cube J8
CCU-9	6 C4v	Spherical-relaxed capped cube
JCSAPR-9	7 C4v	Capped square antiprism J10
CSAPR-9	8 C4v	Spherical capped square antiprism
JTCTPR-9	9 D3h	Tricapped trigonal prism J51
TCTPR-9	10 D3h	Spherical tricapped trigonal prism
JTDIC-9	11 C3v	Tridiminished icosahedron J63
HH-9	12 C2v	Hula-hoop
MFF-9	13 Cs	Muffin

[ML_8]

OP-8	1 D8h	Octagon
HPY-8	2 C7v	Heptagonal pyramid
HBPY-8	3 D6h	Hexagonal bipyramid
CU-8	4 Oh	Cube
SAPR-8	5 D4d	Square antiprism
TDD-8	6 D2d	Triangular dodecahedron
JGBF-8	7 D2d	Johnson gyrobifastigium J26
JETBPY-8	8 D3h	Johnson elongated triangular bipyramid J14
JBTPR-8	9 C2v	Biaugmented trigonal prism J50
BTPR-8	10 C2v	Biaugmented trigonal prism
JSD-8	11 D2d	Snub diphenoid J84
TT-8	12 Td	Triakis tetrahedron
ETBPY-8	13 D3h	Elongated trigonal bipyramid

	Complex **1**	Complex **2**	Complex **3**		Complex **4**	Complex **5**
Structure [ML_9]	Gd1	Tb1	Dy1	Structure [ML_8]	Dy1	Ho1
EP-9	33.368	33.282	33.353	OP-8	30.969	31.101
OPY-9	22.107	22.149	22.260	HPY-8	21.322	21.346
HBPY-9	17.100	17.173	17.093	HBPY-8	14.016	13.934
JTC-9	14.618	14.669	14.562	CU-8	10.766	10.71
JCCU-9	7.743	7.480	7.491	SAPR-8	**1.491**	**1.511**
CCU-9	6.574	6.471	6.411	TDD-8	1.988	2.003
JCSAPR-9	2.588	2.514	2.521	JGBF-8	13.314	13.24
CSAPR-9	1.570	1.634	1.586	JETBPY-8	26.626	26.652
JTCTPR-9	3.524	3.462	3.461	JBTPR-8	2.194	2.191
TCTPR-9	2.763	2.837	2.760	BTPR-8	2.069	2.112
JTDIC-9	12.866	12.930	12.830	JSD-8	3.465	3.463
HH-9	10.620	10.707	10.542	TT-8	11.586	11.539
MFF-9	**1.311**	**1.388**	**1.369**	ETBPY-8	23.607	23.601

Table S3 Continuous Shape Measures calculation for $Co^{II/III}$ in **1–5**

```
-----------------------------------------------------------------------------
 S H A P E   v2.1        Continuous Shape Measures calculation
 (c) 2013  Electronic Structure Group, Universitat de Barcelona
                  Contact:  llunell@ub.edu
-----------------------------------------------------------------------------
```

[ML_6]
HP-6 1 D6h Hexagon
PPY-6 2 C5v Pentagonal pyramid
OC-6 3 Oh Octahedron
TPR-6 4 D3h Trigonal prism
JPPY-6 5 C5v Johnson pentagonal pyramid J2

	Complex **1**	Complex **2**	Complex **3**	Complex **4**		Complex **5**	
Structure [ML_6]	Co1	Co1	Co1	Co1	Co2	Co1	Co2
HP-6	32.486	32.414	32.426	29.656	29.392	29.851	29.222
PPY-6	28.994	29.072	29.177	25.899	25.311	26.298	25.072
OC-6	**0.092**	**0.087**	**0.101**	**0.436**	1.103	**0.363**	1.179
TPR-6	16.086	15.886	16.154	14.051	15.167	14.351	15.13
JPPY-6	32.461	32.537	32.624	29.417	29.525	29.783	29.265

Table S4 Hydrogen bonding parameters for **1–5**

Interactions	Type of H-bond	D–H (Å)	D···A (Å)	H···A (Å)	D–H···A (Å)
Complex **1**					
O6WA···O1	Inter	–	2.9016(17)	–	–
O6WA···O2	Inter	–	3.0030(16)	–	–
O6WA···O5W	Inter	–	2.5330(18)	–	–
O5W–H5WA···O1	Inter	0.85	2.9887(14)	3.00	80
O5W–H5WA···O2W	Inter	0.85	2.8632(21)	2.18	136
O5W–H5WB···O5	Inter	0.85	2.9473(15)	2.74	95
O5W–H5WB···O4W	Inter	0.85	3.0639(16)	2.32	146
O4W–H4WB···O6WA	Inter	0.85	2.8776(18)	2.66	96
O3W–H3WB···O4W	Inter	0.85	2.3555(15)	1.54	158
O3W–H3WA···O9	Inter	0.85	2.7105(13)	1.88	165
O10–H10···O3W	Inter	0.82	2.8843(17)	2.06	179

O1W–H1WA···O3W	Inter	0.86	2.8187(14)	1.96	172
O1W–H1WB···O2W	Inter	0.86	2.7275(12)	1.92	154
O2W–H2WB···O8	Inter	0.85	2.8155(14)	1.97	171
O10···O10	Inter	–	2.749	–	–
Complex **2**					
O6W–H6WA···O1	Inter	0.87	3.0529(19)	2.37	135
O6W–H6WA···O2	Inter	0.87	2.9569(22)	2.15	153
O6W–H6WB···O5W	Inter	0.87	3.0168(19)	2.54	114
O5W–H5WA···O1	Inter	0.87	3.0192(21)	2.47	121
O5W–H5WA···O5	Inter	0.87	2.9025(19)	2.06	163
O5W–H5WB···O2W	Inter	0.87	2.9029(18)	2.15	143
O4W–H4WB···O6W	Inter	0.87	2.7255(18)	2.17	121
O4W–H4WA···O5W	Inter	0.87	2.9555(21)	2.75	94
O3W–H3WB···O4W	Inter	0.87	2.6470(16)	1.80	164
O3W–H2WA···O9	Inter	0.87	2.6907(18)	1.87	156
O10–H10···O3W	Inter	0.84	2.7910(22)	1.95	174
O1W–H1WA···O3W	Inter	0.87	2.8002(16)	2.38	109
O1W–H1WB···O2W	Inter	0.87	2.7004(16)	2.54	91
O2W–H2WA···O8	Inter	0.87	2.8067(20)	1.97	161
O10···O10	Inter	–	2.694	–	–
Complex **3**					
O1W–H1WA···O11	Inter	0.87	2.8723(1)	2.02	166
O1W–H1WB···O2W	Inter	0.87	2.7155(1)	1.87	161
O11–H11···O9	Inter	0.82	2.6665(1)	1.89	156
O10–H10···O11	Inter	0.82	2.8210(1)	2.75	86
O2W–H2WB···O12	Inter	0.85	2.8307(1)	2.01	161
O2W–H2WA···O8	Inter	0.85	2.8208(1)	1.97	179
O12–H12···O1	Inter	0.82	2.8778(1)	2.26	131
O12–H12···O5	Inter	0.82	3.0670(1)	2.33	149

Complex **4**					
O12–H13···O11	Intra	0.95	2.5518(7)	2.02	113
Complex **5**					
O12–H13···O11	Intra	0.95	2.5272(3)	1.99	113

Table S5 The splitting of the lowest multiplets for Tb^{III} ion in **2** and for Ho^{III} ion in **5** calculated in OpenMOLCAS/SINGLE_ANISO together with g-values for selected pseudo-doublets and respective tunneling rates.

Tb^{III}		Ho^{III}	
E (cm^{-1})		E (cm^{-1})	
0	$g_x = 0.000$, $g_y = 0.000$, $g_z = 17.664$	0	$g_x = 0.000$, $g_y = 0.000$, $g_z = 14.992$
0.759	$\Delta_{tun} = 0.759$ cm^{-1}	1.28	$\Delta_{tun} = 1.284$ cm^{-1}
81.7	$g_x = 0.000$, $g_y = 0.000$, $g_z = 13.520$	19.4	$g_x = 0.000$, $g_y = 0.000$, $g_z = 13.676$
86.2	$\Delta_{tun} = 4.512$ cm^{-1}	20.5	$\Delta_{tun} = 1.164$ cm^{-1}
112		118	
123		129	
134		139	
159		143	
179		172	
200		183	
208		216	
297		228	
298		236	
		262	
		273	
		284	
		288	

Table S6 The splitting of the lowest multiplets for Dy^{III} ion in **3** compounds calculated in OpenMOLCAS/SINGLE_ANISO together with g-values for each Kramers doublets and respective transition magnetic moments within each doublet quantifying probability for the quantum tunneling (QTM)

E (cm^{-1})	g_x	g_y	g_z	QTM
0.0	0.158	0.424	19.117	0.0969
66.0	1.737	4.549	13.217	1.2367
109	0.849	3.798	10.465	1.2907
168	0.792	3.702	13.055	1.1968
196	0.442	2.082	15.622	0.5586
217	0.521	4.284	11.720	2.1553
278	0.225	3.411	10.144	2.2887
320	1.031	4.878	15.328	1.2805

Table S7 The splitting of the lowest multiplets for Dy^{III} ion in **4** compounds calculated in OpenMOLCAS/SINGLE_ANISO together with *g*-values for each Kramers doublets and respective transition magnetic moments within each doublet quantifying probability for the quantum tunneling (QTM)

E (cm^{-1})	g_x	g_y	g_z	QTM
0.0	0.359	2.296	15.611	0.4426
19.2	0.630	1.765	14.370	0.5691
138	2.719	3.940	12.790	1.1176
198	8.433	6.417	0.992	1.3767
263	2.645	3.516	14.110	2.3930
288	0.554	1.083	17.844	0.6475
379	0.250	0.443	17.817	0.4472
470	0.061	0.104	19.251	0.0369

Table S8 The splitting of the lowest multiplets for Co^{II} ion in **4** compounds calculated in OpenMOLCAS/SINGLE_ANISO together with *g*-values for each Kramers doublets

E (cm^{-1})	g_x	g_y	g_z
0.0	2.232	2.853	7.405
215	1.431	2.413	4.808
576	3.476	3.305	0.710
927	0.069	0.099	3.22
1323	0.567	0.873	5.547
1445	1.739	2.122	3.511

Table S9 The splitting of the lowest multiplets for Co^{II} ion in **5** compounds calculated in OpenMOLCAS/SINGLE_ANISO together with *g*-values for each Kramers doublets

E (cm^{-1})	g_x	g_y	g_z
0.0	2.250	3.089	7.176
202	1.433	2.111	5.107
603	3.943	3.392	0.914
944	0.023	0.216	3.286
1325	0.535	0.834	5.489
1447	1.731	2.119	3.478